





A comparative high-resolution spectroscopic analysis of in situ and accreted globular clusters

E. Ceccarelli^{1,2} , A. Mucciarelli^{2,1} , D. Massari¹ , M. Bellazzini¹ , and T. Matsuno^{3,4}

¹ INAF - Astrophysics and Space Science Observatory of Bologna, Via Gobetti 93/3, 40129 Bologna, Italy
e-mail: edoardo.ceccarelli3@unibo.it

² Department of Physics and Astronomy, University of Bologna, Via Gobetti 93/2, 40129 Bologna, Italy

³ Astronomisches Rechen-Institut, Zentrum für Astronomie der Universität Heidelberg, Mönchhofstraße 12-14, 69120 Heidelberg, Germany

⁴ Kapteyn Astronomical Institute, University of Groningen, Landleven 12, 9747 AD Groningen, The Netherlands

October 10, 2024

ABSTRACT

Globular clusters (GCs) are extremely intriguing systems that help in reconstructing the assembly of the Milky Way via the characterization of their chemo-chrono-dynamical properties. In this study, we use high-resolution spectroscopic archival data from UVES at VLT and UVES-FLAMES at VLT to compare the chemistry of GCs dynamically tagged as either Galactic (NGC 6218, NGC 6522 and NGC 6626) or accreted from distinct merging events (NGC 362 and NGC 1261 from *Gaia*-Sausage-Enceladus, Ruprecht 106 from the Helmi Streams) in the metallicity regime where abundance patterns of field stars with different origin effectively separate ($-1.3 \leq [\text{Fe}/\text{H}] \leq -1.0$ dex). We find remarkable similarities in the abundances of the two *Gaia*-Sausage-Enceladus GCs across all chemical elements. They both display depletion in the α -elements (Mg, Si and Ca) and statistically significant differences in Zn and Eu compared to in situ GCs. Additionally, we confirm that Ruprecht 106 exhibits a completely different chemical makeup compared to the other target clusters, being underabundant in all chemical elements. This demonstrates that when high precision is achieved, the abundances of certain chemical elements not only can efficiently separate in situ from accreted GCs, but can also distinguish among GCs born in different progenitor galaxies. In the end, we investigate the possible origin of the chemical peculiarity of Ruprecht 106. Given that its abundances do not match the chemical patterns of field stars associated to its most likely parent galaxy (i.e., the Helmi Streams), especially being depleted in the α -elements, we interpret Ruprecht 106 as originating in a less massive galaxy compared to the progenitor of the Helmi Streams.

Key words. Galaxy: globular clusters – stars: abundances — Galaxy: formation — globular clusters: general

1. Introduction

The latest data releases of the ESA/*Gaia* mission (*Gaia* Collaboration et al. 2021, 2023) have instigated a profound transformation in our comprehension of the early chronicles of the Milky Way (MW). This enormous 6-D phase space dataset led to a clearer understanding of the roles played by various mergers in shaping the Galactic halo (see Helmi 2020 for a review), as predicted by simulations in the Λ CDM cosmological framework (White & Frenk 1991, Moore et al. 1999, Helmi & de Zeeuw 2000, Newton et al. 2018). The imprint of accretion events manifest dynamically as stellar streams (Helmi et al. 1999, Ibata et al. 2024), substructures discernible in phase space (e.g., Helmi et al. 2018, Belokurov et al. 2018, Myeong et al. 2018, Koppelman et al. 2019) and dwarf galaxies whose disruption is currently ongoing (Ibata et al. 1994, Majewski et al. 2003). During such events, not only field stars but also globular clusters (GCs) may survive the merging processes, contributing to the formation of the present-day MW GC system (Brodie & Strader 2006, Peñarrubia et al. 2009, Bellazzini et al. 2020, Trujillo-Gomez et al. 2021). Leveraging the extremely precise kinematic data provided by the *Gaia* mission, the orbits of MW GCs have been reconstructed with exceptional precision. Through the analysis of their orbital properties, MW GCs have been classified into distinct groups by several authors (Massari et al. 2019, Forbes 2020, Callingham et al. 2022, Chen & Gnedin 2024), distin-

guishing those accreted from disrupted dwarf galaxies, such as *Gaia*-Sausage-Enceladus (GSE, Belokurov et al. 2018, Helmi et al. 2018), Sequoia (Myeong et al. 2018) or the Helmi Streams (Helmi et al. 1999) from those formed in situ. Complications may arise in the interpretation of these findings due to the complex and overlapping distribution of GCs in orbital parameters spaces (Callingham et al. 2022). This complexity is further exacerbated when accounting for the impact of a non-static potential in the computation of a GC orbit (Amarante et al. 2022, Belokurov et al. 2023, Pagnini et al. 2023, Chen & Gnedin 2024). Nonetheless, it has been established that dynamically tagged groups of GCs lay on different sequences in the age-metallicity space (Kruijssen et al. 2019, Massari et al. 2019, Myeong et al. 2019), confirming the dual nature of the MW GC system in this plane already found in the pre-*Gaia* era (Marín-Franch et al. 2009, Forbes & Bridges 2010, Leaman et al. 2013, VandenBerg et al. 2013). In particular, it has been demonstrated that older systems at fixed metallicity are more likely to be born in galaxies with a higher star formation efficiency, like the MW in its earliest phases, compared to dwarf galaxies (e.g., Massari et al. 2023).

This intricate perspective of the assembly history of the MW can be further enriched by the addition of chemical abundance data, obtained either from high-resolution spectra and from large spectroscopic surveys (Venn et al. 2004, Nissen & Schuster

2010, Helmi et al. 2018, Horta et al. 2020, Minelli et al. 2021, Limberg et al. 2022, Malhan et al. 2022, Naidu et al. 2022a, Horta et al. 2023, Monty et al. 2023a, Ceccarelli et al. 2024). However, when looking at the distribution of GCs in chemical spaces, the differences between these two populations are subtle, making the interpretation of the results not trivial. For instance, Recio-Blanco (2018) highlights a very low scatter in the $[\alpha/\text{Fe}]$ ratio among GCs with $[\text{Fe}/\text{H}] < -0.8$ dex regardless of their origin. On a similar note, Horta et al. (2020) employed the $[\text{Si}/\text{Fe}]$ ratio from APOGEE DR17 (Abdurro'uf et al. 2022) of 46 GCs to explore whether their distribution in chemical spaces reflect the kinematically defined classification by Massari et al. (2019). Interestingly, they observed that the positions of both in-situ and accreted subgroups in this chemical space align with those of their field stars counterparts. However, they were unable to effectively identify different behaviours from GCs that were brought in by separate progenitors, possibly because of the higher precision needed. Recently, Belokurov & Kravtsov (2024) discriminated between Galactic and extragalactic origin for MW GCs using the $[\text{Al}/\text{Fe}]$ ratios, building up on the findings by Belokurov & Kravtsov (2022). However, caution should be exercised when using the abundances of light elements in GCs, owing to the impact of multiple populations (Bastian & Lardo 2018). Finally, Monty et al. (2023a,b) showcased the efficacy of differential chemical analysis on GCs. Their works not only revealed chemical inhomogeneity at a precision level of 0.02 dex for all chemical elements in GCs, but also showed distinctions in the chemical compositions of two GCs, NGC 288 and NGC 362, associated with the same progenitor, GSE. Specifically, NGC 288 and NGC 362 exhibit dissimilarities in their chemical make-ups, particularly in neutron-capture elements. This difference could be interpreted either as stemming from chemical inhomogeneities in the progenitor or as a consequence of internal chemical evolution within the GCs. In light of all the mentioned complexities, which underline the challenges associated with interpreting results when comparing diverse studies, it becomes evident that maintaining homogeneity is imperative in conducting chemical analyses aimed at verifying the origin of GCs.

In this study, we will derive fully homogeneous detailed elemental abundances for several species of six GCs with similar metallicity ($-1.3 \leq [\text{Fe}/\text{H}] \leq -1.0$ dex) consistently associated with different progenitors (see below) by all post-*Gaia* studies (Massari et al. 2019, Forbes 2020, Callingham et al. 2022, Chen & Gnedin 2024). These GCs lie in the metallicity range best suitable for chemical tagging studies, where abundance trends of in situ and accreted objects start to significantly part ways (Nissen & Schuster 2010, Helmi et al. 2018, Matsuno et al. 2022b). Three of the target clusters, namely NGC 362, NGC 1261, and Ruprecht 106 (Rup106 hereafter), lay on the younger branch of the Galactic GCs age-metallicity relation (AMR, Dotter et al. 2010, 2011), that is interpreted as a hint of an accreted origin. Specifically, due to the characteristics in the spaces defined by the integrals of motion, they have been assigned to GSE (NGC 362 and NGC 1261) and the Helmi Streams (Rup106). Also, we selected three targets (NGC 6218, NGC 6522 and NGC 6626) that are generally considered as in situ, since they fit the older branch of the AMR (Dotter et al. 2010, 2011, Villanova et al. 2017, Kerber et al. 2018) and move on a orbits compatible with either the MW disc (NGC 6218) or the Bulge (NGC 6522 and NGC 6626). The primary objective of this work is to test precise chemical tagging as a tool to infer the origin of GCs. When complementing the chrono-dynamical information, chemical tagging might clarify the differences among clusters with ambiguous associations. Furthermore, it enables determining if the progenitor

galaxy and the associated GC candidates are chemically compatible. For this to be effective, the combination of high precision in abundances derivation, which can only be achieved using high-quality data, and homogeneity in the detailed analysis is required. This is why we reanalyze these six clusters, which have extensively been studied in the literature, to compare them with each other with the utmost precision.

The paper is structured as follows. In Section 2 we list the observation that were collected to compile the spectroscopic dataset. In Section 3 we describe the methodology employed to carry out the chemical analysis. In Section 4 we show the output of the analysis. In Section 5 we compare our results with literature. In Section 6 we discuss the peculiarity of Ruprecht 106. In Section 7 we recap the main results of this work.

2. Observations

We retrieved our entire spectroscopic dataset from the ESO archive. The spectra of all the stars have been acquired using the multi-object spectrograph UVES-FLAMES (Pasquini et al. 2002) or UVES (Dekker et al. 2000) mounted at the Very Large Telescope (VLT) of the European Southern Observatory. Stars have been observed using the Red Arm 580 CD3 grating with a spectral coverage between 4800 and 6800 Å and a spectral resolution of $R=40,000$. Typical signal-to-noise ratios for these spectra are in the range of $40 \leq S/N \leq 65$ at 5000 Å and $60 \leq S/N \leq 90$ at 6000 Å. The spectra were reduced using the dedicated ESO pipeline¹ that includes bias subtraction, flat-fielding, wavelength calibration, spectral extraction and order merging. For the stars observed with UVES at VLT, the contribution of the sky has been properly removed from each stellar spectrum during the pipeline reduction. For the stars observed with UVES-FLAMES at VLT, the sky contribution have been taken into account by acquiring the spectra of some nearby sky regions at the same time as the science targets and subtracting it to each individual exposure. In the end, single exposures of the same star have been merged to obtain the final spectrum for each target. We display in Fig. 1 the spectra of six stars, one per target cluster, to showcase the quality of the dataset.

As mentioned in the Introduction, the sample of GCs subject of this study has been selected based on their similar metallicity and on their dynamical association (always consistent among different studies, e.g., Massari et al. 2019, Forbes 2020, Callingham et al. 2022, see below). The individual spectroscopic targets analysed in this work has been selected as follows:

- NGC 362. This cluster has been categorized as accreted during the merger with GSE. The mean metallicity of NGC 362 is $[\text{Fe}/\text{H}] = -1.17 \pm 0.05$ dex (Carretta et al. 2013). We collected the spectra of 14 RGB stars observed under the ESO-VLT Programme 083.D-0208 (PI: E. Carretta).
- NGC 1261. This GC has also been associated with the GSE accretion event. The mean metallicity of this cluster is $[\text{Fe}/\text{H}] = -1.28 \pm 0.02$ dex (Marino et al. 2021). Our dataset includes the spectra of 12 RGB stars. Among them, 6 were observed under the ESO-VLT Programme 0101.D-0109 (PI: A. Marino), 4 were observed under the ESO-VLT Programme 197.B-1074 (PI: G. F. Gilmore) and 2 were observed under the ESO-VLT Programme 193.D-0232 (PI: F. R. Ferraro).
- NGC 6218. This system is an in-situ GC located in the MW disc. NGC 6218 has a mean metallicity of $[\text{Fe}/\text{H}] = -1.33 \pm$

¹ <https://www.eso.org/sci/software/pipelines/>

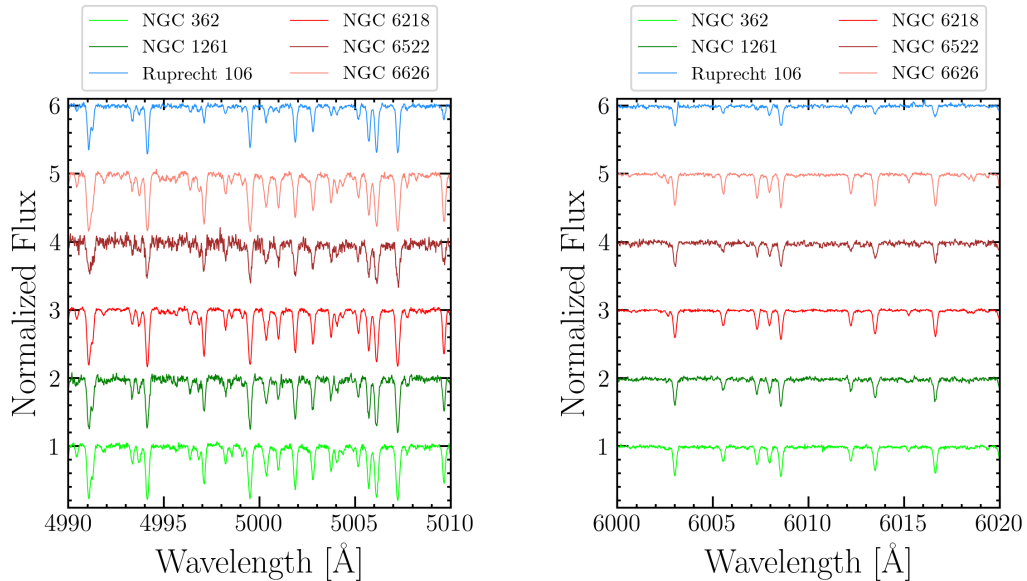


Fig. 1. Spectra of stars from the six target clusters observed with UVES at VLT and UVES-FLAMES at VLT at different wavelengths. The spectra have been vertically shifted for sake of clarity.

0.08 dex (Carretta et al. 2009). We include in our analysis 11 RGB stars observed under the ESO-VLT Programme 073.D-0211 (PI: E. Carretta).

- NGC 6522. This is an in situ cluster placed in the MW Bulge. Its mean metallicity is $[\text{Fe}/\text{H}] = -1.16 \pm 0.05$ dex (Barbuy et al. 2021). Our sample is composed of 4 RGB stars observed under the ESO-VLT Programme 097.D-0175 (PI: B. Barbuy).
- NGC 6626. This is also an in-situ MW Bulge globular cluster with a mean metallicity of $[\text{Fe}/\text{H}] = -1.29 \pm 0.01$ dex (Villanova et al. 2017). We collected the spectra of 16 RGB stars observed under the ESO-VLT Programme 091.D-0535 (PI: C. Moni Bidin).
- Ruprecht 106. Among the population of accreted GCs, one that has always gathered great attention in the community is Rup106. Its orbit is typical of the Galactic halo (Freijij et al. 2021) and due to its positioning in the spaces defined by the integrals of motion, this GC has been tentatively linked with the progenitor of the Helmi Streams. The chemical peculiarity of Rup106 has been revealed by several spectroscopic analyses (e.g., Brown et al. 1997, Villanova et al. 2013, V13 hereafter), which find that all Rup106 target spectra are depleted in $[\alpha/\text{Fe}]$ compared to GCs and field stars of the same metallicity, that is $[\text{Fe}/\text{H}] = -1.37 \pm 0.11$ dex (Lucertini et al. 2023). We collected the spectra of 9 RGB stars that have been observed under the ESO-VLT Programme 069.D-0642 (PI: P. François).

3. Chemical analysis

3.1. Stellar parameters

We derived both the effective temperature (T_{eff}) and the surface gravity ($\log g$) exploiting the *Gaia* Data Release 3 (DR3, Gaia Collaboration et al. 2023) photometric dataset. It is important to note that stars in GCs are located at significant distances and within crowded environments, which may result in a slight

degradation of the quality of *Gaia* photometry. Stars with $\text{ruwe} > 1.4$ were flagged because their photometry might be of lower quality (Gaia Collaboration et al. 2021).

T_{eff} have been determined using the empirically calibrated $(\text{BP} - \text{RP})_0 - T_{\text{eff}}$ relation provided by Mucciarelli et al. (2021a). The choice of using the $(\text{BP} - \text{RP})$ color is guided by the fact that it is the most extended in wavelength among *Gaia* colors, thus ensuring an optimal sampling of the spectral energy distribution. This approach also eliminates the need to rely on measurements from other photometric systems, which may have lower precision than *Gaia*. We checked that using other *Gaia* colours would result in T_{eff} differences always smaller than 50 K, which is below the current uncertainties. The color excess $E(\text{B}-\text{V})$ adopted for each GC is taken from Harris (2010). Given the high extinction in the direction of the Galactic bulge, we corrected the *Gaia* photometry of NGC 6522 and NGC 6626 for effects of differential reddening following the prescription described in Milone et al. (2012), using the Cardelli et al. (1989) extinction law. This analysis was performed on the catalogues provided by Vasiliev & Baumgardt (2021), focusing only on stars with a probability membership $> 90\%$. The effects of the extinction on the observed color $(\text{BP} - \text{RP})$ have been taken into account following the iterative prescription described in Gaia Collaboration et al. (2018). Since the color - T_{eff} relation we employed is sensitive to the metallicity of the star, we assumed the $[\text{Fe}/\text{H}]$ value listed in the Harris (2010) catalogue as representative of the GC under investigation to get an initial estimate of T_{eff} . We note that estimating the T_{eff} using the derived $[\text{Fe}/\text{H}]$ values leads to variations from the initial values always lower than 20 K. Internal errors in T_{eff} due to the uncertainties in photometric data, reddening and assumed color - T_{eff} relation are in the range 80 - 110 K.

Surface gravities have been estimated from the Stefan-Boltzmann relation, using the photometric T_{eff} and a representative stellar mass of $0.8 M_{\odot}$, typical for RGB stars in old isochrones at this metallicity, the G-band bolometric corrections described by Andrae et al. (2018), and the distance provided by

Table 1. Stellar parameters for the selected targets: star ID from previous literature works, ID from *Gaia* DR3, derived effective temperature, surface gravity, and microturbulent velocity. Last column is a flag to check the quality of the *Gaia* photometry of the star (flag_high_ruwe=0 stands for ruwe < 1.4). The complete table is available in electronic form.

Cluster	Star ID	ID <i>Gaia</i> DR3	T_{eff} (K)	log g (dex)	v_t (km s ⁻¹)	flag_high_ruwe
NGC 362	1037	4690839791797266688	4549	1.35	1.4	0
NGC 362	1840	4690841273563721728	4485	1.28	1.5	0
NGC 362	2683	4690886834576765952	4142	0.69	1.6	0
NGC 362	3392	4690888105887037184	4522	1.33	1.5	0
NGC 362	5012	4690887590491024768	4527	1.32	1.4	0
...

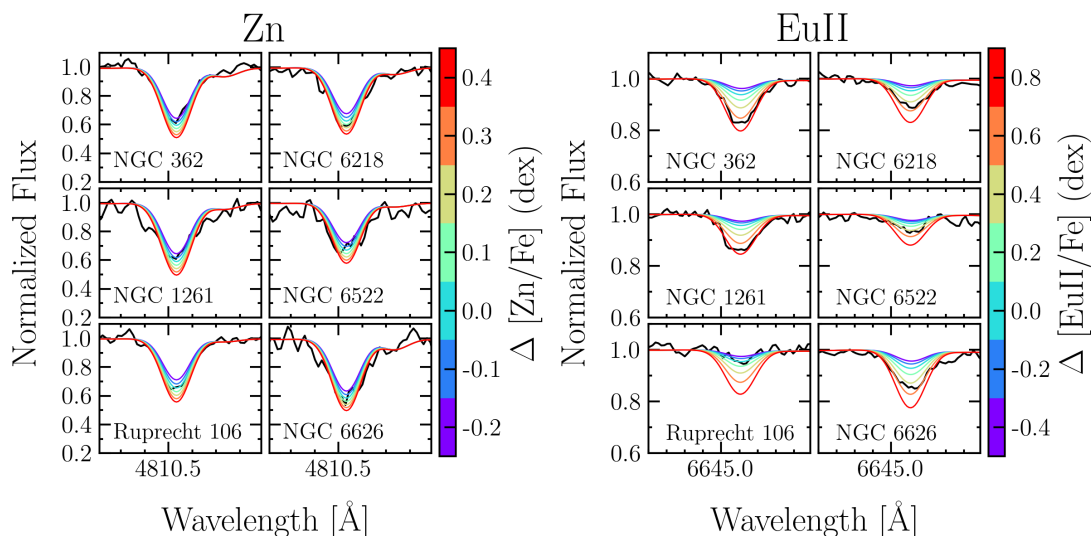


Fig. 2. Comparison around the 4810.5 Å Zn (left panel) and the 6645.1 Å EuII (right panel) lines between the observed spectra and seven synthetic spectra computed assuming the derived atmospheric parameters for each star and varying the level of [Zn/Fe] and [EuII/Fe]. The variations are computed with respect to the abundances measured in Rup106.

Baumgardt & Vasiliev (2021). The uncertainties on the log g are derived through the propagation of the errors on T_{eff} , photometry and distance, and they are always under 0.1 dex.

In the end, we calculated microturbulent velocities (v_t) by minimizing the trend between iron abundances and reduced equivalent widths, defined as $\log_{10}(\text{EW}/\lambda)$. To do so, we used on average ≥ 100 iron lines per star. We assumed a conservative uncertainty of 0.2 km s⁻¹. All the atmospheric parameters are listed in Table 1.

3.2. Deriving the abundances

The determination of chemical abundances of Mg, Si, Ca, TiI, TiII, Cr, Fe, Ni, and Zn was conducted by means of a comparative analysis between the observed equivalent widths (EWs), measured with the code DAOSPEC (Stetson & Pancino 2008) through the automatic tool 4DAO (Mucciarelli 2013), and theoretical line strengths. This analysis was executed using the code GALA (Mucciarelli et al. 2013).

We employed the spectral synthesis using the proprietary code SALVADOR to derive the chemical abundances for the species that have hyperfine/isotopic splitting transitions (ScII, V, Mn, Co, Cu, YII, BaII, LaII, and EuII). SALVADOR runs a χ^2 -minimization between the observed line and a grid of suitable synthetic spectra computed on-the-fly by the code SYNTH (Kurucz 2005) varying only the abundance of the matching element and keeping the stellar parameters fixed. Synthetic spectra were

computed using all the atomic and molecular transitions available in the Kurucz/Castelli² database.

We used ATLAS9 (Kurucz 2005) model atmospheres computed assuming plane-parallel geometry, hydrostatic and radiative equilibrium, and local thermodynamic equilibrium for all the chemical elements. We started from an α -enhanced model atmosphere ($[\alpha/\text{Fe}] = +0.4$ dex) for all the target GCs except for Rup106 for which we used a solar-scaled chemical mixture, according to the values of $[\alpha/\text{Fe}]$ we derived. Examples of fits around absorption lines of elements of interest (i.e. Zn and EuII, see Sections 4.2 and 4.3) are displayed in Figure 2. Different synthetic spectra are computed for each star by assuming the atmospheric parameters derived as described in Section 3.1, and varying the abundances of Zn and EuII.

Finally, we scale the abundance ratios to the solar values using the chemical composition described in Grevesse & Sauval (1998), since ATLAS9 model atmospheres are computed based on this solar mixture (Castelli & Kurucz 2003).

3.3. Abundance uncertainties

During the determination of the uncertainties associated with abundance ratios, it is imperative to account for two principal sources of error: first, internal errors stemming from the measurement of the EW, and second, errors originating from the selection of atmospheric parameters.

² <http://wwwuser.oats.inaf.it/castelli/linelists.html>

The uncertainties attributed to EW measurements have been estimated as the dispersion observed around the mean of individual line measurements, divided by the root mean square of the number of lines employed in the analysis.

The internal error on chemical abundances derived with spectral synthesis have been quantified using Monte Carlo simulations. To do so, we repeated the analysis on 1000 noisy synthetic spectra obtained adding Poissonian noise in order to mimic the S/N of the real spectra. The uncertainty is estimated as the standard deviation of the abundance distribution of the 1000 noisy synthetic spectra.

Finally, we performed new calculations of the chemical abundances, considering also the uncertainties associated with the atmospheric parameters. This involved varying one stellar parameter at a time while keeping the others fixed. In the end, all the sources of error are added in quadrature. Given that our chemical abundances are expressed as abundance ratios ($[X/Fe]$), the uncertainties on the iron abundance $[Fe/H]$ have been taken into account.

The total uncertainty has been estimated as the squared sum of these two components. Therefore, the final errors have been calculated as:

$$\sigma_{[Fe/H]} = \sqrt{\frac{\sigma_{Fe}^2}{N_{Fe}} + (\delta_{Fe}^{T_{\text{eff}}})^2 + (\delta_{Fe}^{\log g})^2 + (\delta_{Fe}^{v_i})^2} \quad (1)$$

$$\sigma_{[X/Fe]} = \sqrt{\frac{\sigma_X^2}{N_X} + \frac{\sigma_{Fe}^2}{N_{Fe}} + (\delta_X^{T_{\text{eff}}} - \delta_{Fe}^{T_{\text{eff}}})^2 + (\delta_X^{\log g} - \delta_{Fe}^{\log g})^2 + (\delta_X^{v_i} - \delta_{Fe}^{v_i})^2} \quad (2)$$

where $\sigma_{X,Fe}$ is the dispersion around the mean of chemical abundances, $N_{X,Fe}$ is the number of used lines and $\delta_{X,Fe}^i$ are the abundance differences obtained by varying the parameter i .

4. Abundances of target GCs

In this section, we discuss abundances of α -, iron-peak, and neutron-capture elements of target GCs. We exercise caution when interpreting the abundances of certain chemical elements that may be influenced by the presence of multiple populations within GCs (e.g., O, Na, Mg, and Al, see Bastian & Lardo 2018). Among these species, we selectively focus only on Mg, which exhibits minimal dispersion within five out of six GC in our sample. This outcome aligns with expectations, particularly considering that targeted systems belong to the low-mass and high metallicity regime of the MW GC system, where the efficiency of the MgAl burning channel diminishes (Ventura et al. 2013, Dell'Agli et al. 2018, Alvarez Garay et al. 2024). Indeed, we find spread in the $[Mg/Fe]$ distribution of stars only in the most massive among our target cluster, NGC 6626. Since we only care about the pristine chemical composition of the gas that formed the cluster, we derived the mean value of $[Mg/Fe]$ only selecting first generation stars. The results obtained from the homogeneous chemical analysis of 66 RGB stars of the sample of six GCs are listed in Tables 2 - 4. Mean abundances for each GC are available in Table 5. The average abundance ratios of the target GCs are illustrated in Figures 3 - 5.

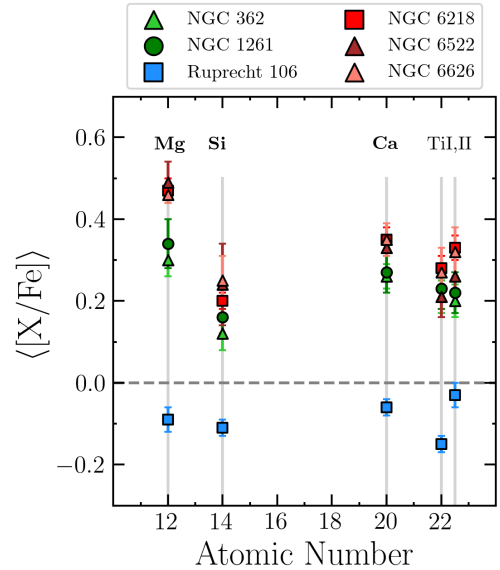


Fig. 3. Comparison of mean abundance ratios of the α -elements $[Mg/Fe]$, $[Si/Fe]$, $[Ca/Fe]$, $[TiI/Fe]$, and $[TiII/Fe]$ for target GCs NGC 362 (green triangles), NGC 1261 (dark green circles), NGC 6218 (red squares), NGC 6522 (brown triangles), NGC 6626 (pink triangles), and Rup106 (blue squares). Errorbars indicate the standard deviation.

4.1. α -elements

In Figure 3 we show the mean values of the α -elements abundances. These chemical elements are predominantly synthesized in massive stars and subsequently dispersed into the interstellar medium through core-collapse supernovae events (CC-SNe, Kobayashi & Nomoto 2009, Romano et al. 2010, Kobayashi et al. 2020). Additionally, there is a minor but discernible contribution from Type Ia supernovae (SNe Ia), particularly notable for Ca and Ti, as discussed in Kobayashi et al. (2020).

First of all, we find that the two GCs associated to GSE (green filled symbols) show identical abundances, within the uncertainties, in all the analysed α -elements. Second, we show that mean abundances of Mg, Si and Ca of the three in situ GCs NGC 6218, NGC 6522 and NGC 6626 (red, brown and pink filled symbols, respectively) are fully compatible among each other. Ti is the element where such a consistency is less evident. Third, we find that NGC 362 and NGC 1261 are α -depleted compared to the in situ GCs. They display differences in the α -element at the 1σ level in Mg and Ca when comparing the average abundances and the respective standard deviations (see Appendix A.1 for a comparison with literature). Last, we derive subsolar abundances in the α -elements of Rup106 (blue filled squares), specifically with $[\alpha/Fe] \sim -0.1$ dex, in good agreement with literature works (Brown et al. 1997, V13, see Appendix A.2 for a comparison with the results by V13). This is, on average, 0.3 – 0.4 dex lower than the other five target clusters.

These results are particularly relevant in understanding to which degree can we use α -elements to distinguish the origin of GCs. The observed trend matches well the expectations given by the cluster chrono-dynamical associations. Indeed, GSE clusters NGC 1261 and NGC 362 share the same α -element abundances, as expected for clusters accreted from the same progenitor, with lower $[\alpha/Fe]$ values compared to NGC 6218, NGC 6522 and

Table 2. Chemical abundances for the α -elements for the target stars. The entire table is available in electronic form.

Cluster	Star ID	[Fe/H] (dex)	[Mg/Fe] (dex)	[Si/Fe] (dex)	[Ca/Fe] (dex)	[Ti/Fe] (dex)	[TiII/Fe] (dex)
NGC 362	1037	-1.04 ± 0.09	0.28 ± 0.04	0.10 ± 0.10	0.27 ± 0.05	0.20 ± 0.09	0.21 ± 0.12
NGC 362	1840	-1.04 ± 0.09	0.25 ± 0.04	0.08 ± 0.10	0.22 ± 0.06	0.18 ± 0.10	0.17 ± 0.11
NGC 362	2683	-1.12 ± 0.06	0.36 ± 0.05	0.20 ± 0.11	0.30 ± 0.08	0.24 ± 0.15	0.21 ± 0.11
NGC 362	3392	-1.07 ± 0.09	0.28 ± 0.03	0.11 ± 0.10	0.24 ± 0.05	0.17 ± 0.09	0.22 ± 0.12
NGC 362	5012	-1.04 ± 0.09	0.30 ± 0.04	0.14 ± 0.10	0.26 ± 0.06	0.20 ± 0.09	0.20 ± 0.12
...

Table 3. Chemical abundances for the iron-peak elements for the target stars. The entire table is available in electronic form.

Cluster	Star ID	[ScII/Fe] (dex)	[V/Fe] (dex)	[Cr/Fe] (dex)	[Mn/Fe] (dex)
NGC 362	1037	-0.03 ± 0.08	0.09 ± 0.18	-0.01 ± 0.09	-0.26 ± 0.15
NGC 362	1840	-0.04 ± 0.07	0.08 ± 0.18	-0.04 ± 0.09	-0.22 ± 0.15
NGC 362	2683	0.01 ± 0.07	0.13 ± 0.18	0.12 ± 0.12	-0.20 ± 0.15
NGC 362	3392	-0.07 ± 0.08	0.06 ± 0.18	-0.01 ± 0.08	-0.27 ± 0.15
NGC 362	5012	0.05 ± 0.07	0.13 ± 0.18	-0.04 ± 0.09	-0.21 ± 0.15
...
Cluster	Star ID	[Co/Fe] (dex)	[Ni/Fe] (dex)	[Cu/Fe] (dex)	[Zn/Fe] (dex)
NGC 362	1037	0.01 ± 0.13	-0.21 ± 0.04	-0.26 ± 0.18	-0.20 ± 0.15
NGC 362	1840	0.03 ± 0.13	-0.22 ± 0.04	-0.27 ± 0.18	-0.27 ± 0.14
NGC 362	2683	-0.02 ± 0.13	-0.31 ± 0.04	-0.15 ± 0.18	-0.39 ± 0.13
NGC 362	3392	0.00 ± 0.13	-0.14 ± 0.04	-0.31 ± 0.18	-0.24 ± 0.14
NGC 362	5012	0.04 ± 0.13	-0.26 ± 0.04	-0.16 ± 0.18	-0.19 ± 0.15
...

Table 4. Chemical abundances for the neutron-capture elements for the target stars. The entire table is available in electronic form.

Cluster	Star ID	[YII/Fe] (dex)	[BaII/Fe] (dex)	[LaII/Fe] (dex)	[EuII/Fe] (dex)
NGC 362	1037	-0.01 ± 0.15	0.27 ± 0.17	0.15 ± 0.05	0.51 ± 0.05
NGC 362	1840	-0.05 ± 0.15	0.24 ± 0.17	0.13 ± 0.05	0.50 ± 0.04
NGC 362	2683	0.05 ± 0.15	0.28 ± 0.17	0.16 ± 0.05	0.52 ± 0.04
NGC 362	3392	-0.10 ± 0.15	0.19 ± 0.17	0.12 ± 0.05	0.44 ± 0.05
NGC 362	5012	0.12 ± 0.15	0.38 ± 0.17	0.19 ± 0.05	0.55 ± 0.04
...

NGC 6626. In fact, the in situ GCs consistently show higher $[\alpha/\text{Fe}]$ abundances, as predicted for systems born in the MW at this metallicity, where the contribution of SNIa to the gas chemical enrichment was not yet significant. Finally, Rup106 has even lower $[\alpha/\text{Fe}]$ compared to the other target GCs, differentiating from the trends displayed by GSE GCs, indicating an even more different birth environment, probably characterised by a very low star formation efficiency.

4.2. Iron-peak elements

Iron-peak elements primarily originate in Type II CC-SNe and hypernovae (HNe), with some contribution also from SNe Ia. Specifically, elements like Sc, Cu, and Zn are predominantly synthesized by massive stars, while for V and Co the contribution of SNe Ia is not negligible. On the other hand, Cr, Mn, and Ni are primarily produced by SNe Ia (Romano et al. 2010, Kobayashi et al. 2020).

The results shown in Figure 4 indicate that most of the iron-peak elements do not provide effective and clear discrimination between in situ and GSE clusters. Indeed, target GCs display coherent values in all the chemical spaces with the exception once

again of Rup106, which is underabundant in ScII, V, Mn, Co, and Ni. In the bottom panel of Figure 4 we highlight the two elements where Rup106 is most depleted compared to the other systems. Specifically, Cu is the most underabundant among the chemical elements derived in this work ($[\text{Cu}/\text{Fe}] = -0.95$ dex for Rup106). Such low values of $[\text{Cu}/\text{Fe}]$ can be reproduced in stellar systems with chemical evolutionary model assuming very inefficient star formation (star formation rate $< 5 \times 10^{-4} M_{\odot} \text{ yr}^{-1}$, Mucciarelli et al. 2021b). Thus, the pronounced depletion in all of these elements might indicate that Rup106 was born in an environment where the contribution of massive stars was extremely low.

Among the iron-peak elements, the only one demonstrating a statistically significant difference between accreted and in situ GCs is Zn: all the in-situ GCs are overabundant with respect to GSE GCs and Rup106 at the 1σ level. In passing, we note that NGC 6626 shows a significant spread in $[\text{Zn}/\text{Fe}]$, as already found in Villanova et al. (2017). Zn seems therefore a good tracer of the in situ or accreted origin of GCs, but it is not sensitive enough to help distinguishing among different accreted progenitors. Such a conclusion has been drawn also by Minelli et al. (2021), even though they use a sample of GCs at higher metal-

Table 5. Mean abundances ratios for the six GCs analyzed in this work. The standard deviation is reported inside the brackets.

Element	NGC 362	NGC 1261	NGC 6218
$\langle[\text{Fe}/\text{H}]\rangle$	-1.06 ± 0.01 (0.03)	-1.14 ± 0.02 (0.06)	-1.24 ± 0.01 (0.02)
$\langle[\text{Mg}/\text{Fe}]\rangle$	0.30 ± 0.01 (0.04)	0.34 ± 0.02 (0.06)	0.47 ± 0.01 (0.03)
$\langle[\text{Si}/\text{Fe}]\rangle$	0.12 ± 0.01 (0.04)	0.16 ± 0.01 (0.04)	0.20 ± 0.01 (0.02)
$\langle[\text{Ca}/\text{Fe}]\rangle$	0.26 ± 0.01 (0.03)	0.27 ± 0.01 (0.05)	0.35 ± 0.01 (0.03)
$\langle[\text{ScII}/\text{Fe}]\rangle$	-0.02 ± 0.01 (0.03)	0.00 ± 0.01 (0.04)	0.08 ± 0.01 (0.02)
$\langle[\text{Ti}/\text{Fe}]\rangle$	0.21 ± 0.01 (0.04)	0.23 ± 0.01 (0.05)	0.28 ± 0.01 (0.03)
$\langle[\text{TiII}/\text{Fe}]\rangle$	0.20 ± 0.01 (0.04)	0.22 ± 0.01 (0.05)	0.33 ± 0.01 (0.03)
$\langle[\text{V}/\text{Fe}]\rangle$	0.09 ± 0.01 (0.04)	0.10 ± 0.02 (0.07)	0.10 ± 0.02 (0.05)
$\langle[\text{Cr}/\text{Fe}]\rangle$	0.04 ± 0.01 (0.05)	0.01 ± 0.01 (0.04)	-0.02 ± 0.01 (0.04)
$\langle[\text{Mn}/\text{Fe}]\rangle$	-0.23 ± 0.01 (0.03)	-0.29 ± 0.01 (0.05)	-0.33 ± 0.01 (0.04)
$\langle[\text{Co}/\text{Fe}]\rangle$	-0.01 ± 0.01 (0.03)	0.02 ± 0.01 (0.04)	0.10 ± 0.01 (0.04)
$\langle[\text{Ni}/\text{Fe}]\rangle$	-0.25 ± 0.01 (0.05)	-0.21 ± 0.02 (0.06)	-0.15 ± 0.01 (0.03)
$\langle[\text{Cu}/\text{Fe}]\rangle$	-0.21 ± 0.02 (0.06)	-0.22 ± 0.02 (0.08)	-0.15 ± 0.02 (0.08)
$\langle[\text{Zn}/\text{Fe}]\rangle$	-0.30 ± 0.02 (0.06)	-0.23 ± 0.01 (0.05)	-0.02 ± 0.02 (0.05)
$\langle[\text{YII}/\text{Fe}]\rangle$	-0.01 ± 0.03 (0.11)	-0.09 ± 0.03 (0.10)	0.15 ± 0.02 (0.08)
$\langle[\text{BaII}/\text{Fe}]\rangle$	0.28 ± 0.03 (0.11)	0.16 ± 0.03 (0.10)	0.24 ± 0.02 (0.06)
$\langle[\text{LaII}/\text{Fe}]\rangle$	0.14 ± 0.02 (0.07)	0.12 ± 0.01 (0.03)	0.04 ± 0.01 (0.03)
$\langle[\text{EuII}/\text{Fe}]\rangle$	0.52 ± 0.01 (0.05)	0.50 ± 0.02 (0.09)	0.25 ± 0.01 (0.04)
Element	NGC 6522	NGC 6626	Ruprecht 106
$\langle[\text{Fe}/\text{H}]\rangle$	-1.07 ± 0.01 (0.05)	-1.11 ± 0.01 (0.06)	-1.30 ± 0.01 (0.05)
$\langle[\text{Mg}/\text{Fe}]\rangle$	0.49 ± 0.03 (0.05)	0.46 ± 0.01 (0.02)	-0.09 ± 0.01 (0.03)
$\langle[\text{Si}/\text{Fe}]\rangle$	0.24 ± 0.05 (0.10)	0.25 ± 0.02 (0.06)	-0.11 ± 0.01 (0.02)
$\langle[\text{Ca}/\text{Fe}]\rangle$	0.33 ± 0.01 (0.02)	0.35 ± 0.01 (0.04)	-0.06 ± 0.01 (0.02)
$\langle[\text{ScII}/\text{Fe}]\rangle$	-0.04 ± 0.02 (0.05)	0.04 ± 0.01 (0.04)	-0.37 ± 0.01 (0.03)
$\langle[\text{Ti}/\text{Fe}]\rangle$	0.21 ± 0.03 (0.05)	0.27 ± 0.01 (0.06)	-0.15 ± 0.01 (0.02)
$\langle[\text{TiII}/\text{Fe}]\rangle$	0.26 ± 0.03 (0.07)	0.32 ± 0.01 (0.06)	-0.03 ± 0.01 (0.03)
$\langle[\text{V}/\text{Fe}]\rangle$	-0.03 ± 0.01 (0.03)	0.05 ± 0.02 (0.07)	-0.34 ± 0.01 (0.04)
$\langle[\text{Cr}/\text{Fe}]\rangle$	-0.02 ± 0.05 (0.10)	-0.03 ± 0.02 (0.08)	-0.12 ± 0.01 (0.03)
$\langle[\text{Mn}/\text{Fe}]\rangle$	-0.40 ± 0.02 (0.04)	-0.35 ± 0.01 (0.05)	-0.42 ± 0.03 (0.08)
$\langle[\text{Co}/\text{Fe}]\rangle$	0.03 ± 0.01 (0.01)	-0.08 ± 0.01 (0.03)	-0.31 ± 0.02 (0.05)
$\langle[\text{Ni}/\text{Fe}]\rangle$	-0.18 ± 0.01 (0.01)	-0.14 ± 0.01 (0.04)	-0.41 ± 0.01 (0.03)
$\langle[\text{Cu}/\text{Fe}]\rangle$	-0.44 ± 0.05 (0.11)	-0.17 ± 0.02 (0.07)	-0.95 ± 0.02 (0.06)
$\langle[\text{Zn}/\text{Fe}]\rangle$	0.07 ± 0.04 (0.08)	-0.03 ± 0.04 (0.15)	-0.24 ± 0.03 (0.09)
$\langle[\text{YII}/\text{Fe}]\rangle$	-0.18 ± 0.09 (0.18)	0.01 ± 0.02 (0.08)	-0.73 ± 0.01 (0.03)
$\langle[\text{BaII}/\text{Fe}]\rangle$	0.12 ± 0.05 (0.10)	0.07 ± 0.02 (0.07)	-0.11 ± 0.02 (0.07)
$\langle[\text{LaII}/\text{Fe}]\rangle$	0.22 ± 0.10 (0.18)	0.02 ± 0.01 (0.04)	-0.33 ± 0.03 (0.09)
$\langle[\text{EuII}/\text{Fe}]\rangle$	0.18 ± 0.06 (0.09)	0.26 ± 0.02 (0.09)	-0.20 ± 0.04 (0.12)

licity. Indeed, high $[\text{Zn}/\text{Fe}]$ ratios are expected for in situ GCs, and the rationale lies in the fact that the primary contributors to Zn production are hypernovae, which are linked to stars with masses around 25 – 30 M_{\odot} (Romano et al. 2010, Kobayashi et al. 2020). Consequently, galaxies with lower star formation rate should manifest lower $[\text{Zn}/\text{Fe}]$ ratios due to the reduced impact of massive stars (Yan et al. 2020).

4.3. Neutron-capture elements

Slow (s -) neutron-capture elements are mainly synthesized in Asymptotic Giant Branch (AGB) stars. In particular, light s -process elements, (e.g., Y), are produced to a large extent by intermediate-mass AGB stars. Conversely, heavy s -process elements (e.g., Ba, La) are mainly produced in AGB stars with masses lower than 4 M_{\odot} (Kobayashi et al. 2020). Rapid (r -) neutron-capture elements (e.g., Eu), are synthesized during a broad spectrum of events, like special types of CC-SNe (rCC-SNe, e.g., magnetorotational SNe, collapsars, Mösta et al. 2018, Siegel et al. 2019, Kobayashi et al. 2020) and neutron-star mergers (NSM, Lattimer & Schramm 1974).

First of all, we observe that the in situ NGC 6218 is enhanced (≥ 0.2 dex) in $[\text{YII}/\text{Fe}]$ compared to the other two in situ GCs and two GSE GCs. Additionally, among the neutron-capture elements, this is the chemical space in which Rup106 is the most depleted (see bottom panel of Figure 4). This finding is particularly intriguing, as Cu, the other element where Rup106 is notably depleted, is also produced by massive stars through weak s -processes, with a small contribution also by AGB stars (Kobayashi & Nomoto 2009, Kobayashi et al. 2020). Thus, if the lack of weak s -process products is responsible for the low Cu derived, it is also expected that light neutron-capture elements would be similarly depleted, as it is observed for Y.

When examining the abundances of the other neutron-capture elements (see Figure 5), the most notable distinctions between various GCs arise in the r -process element Eu. The two GSE GCs exhibit values that are ~ 0.3 dex higher compared to in situ GCs. The enhancement in r -process of NGC 362 and NGC 1261 has also been highlighted by Monty et al. (2023b) and by Koch-Hansen et al. (2021) respectively, and it resembles the behaviour of GSE field stars at this metallicity (Nissen & Schuster 2011, Fishlock et al. 2017, Aguado et al. 2021, Matsuno et al. 2021, Naidu et al. 2022b) and that of surviving dwarf

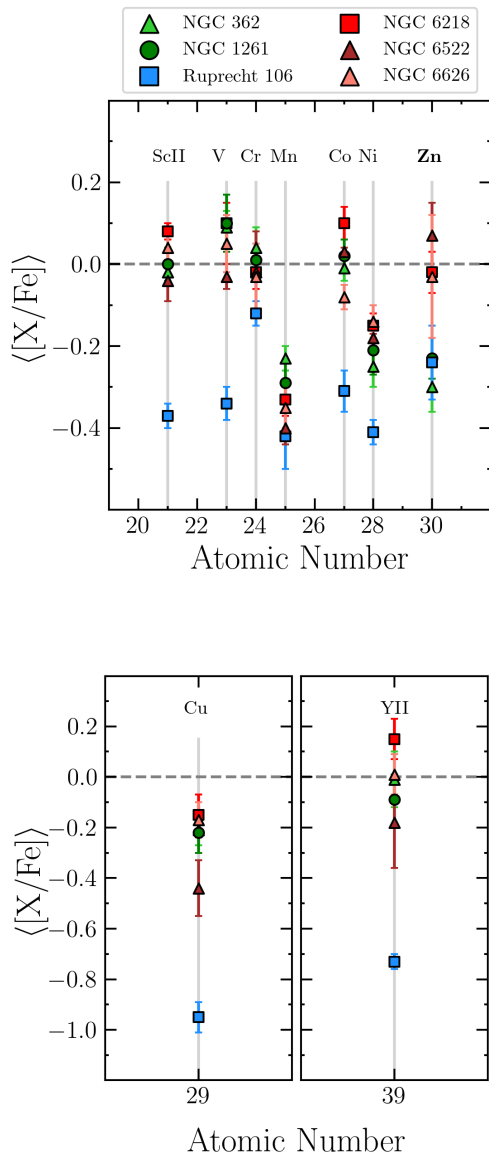


Fig. 4. Comparison of mean abundance ratios of the iron-peak elements $[\text{ScII}/\text{Fe}]$, $[\text{V}/\text{Fe}]$, $[\text{Cr}/\text{Fe}]$, $[\text{Mn}/\text{Fe}]$, $[\text{Co}/\text{Fe}]$, $[\text{Ni}/\text{Fe}]$, and $[\text{Zn}/\text{Fe}]$ for target GCs (top panel). In the bottom panel we plot the two elements ($[\text{Cu}/\text{Fe}]$ and $[\text{YII}/\text{Fe}]$) with the largest differences observed for Rup106. The color coding is the same as in Figure 3. Errorbars indicate the standard deviation.

galaxies, like the LMC, Sculptor and Fornax (Tolstoy et al. 2009, Letarte et al. 2010, Van der Swaelmen et al. 2013, Lemasle et al. 2014). This might be explained by a joint effect of the different star formation efficiency in the progenitor galaxy and the impact of delayed r -process sources (i.e. NSMs), with minimum delay times of the order of 10 - 1000 Myr in producing Eu (Cescutti et al. 2015, Siegel et al. 2019, Naidu et al. 2022b, Ou et al. 2024). Once again, Rup106 is 0.3 – 0.6 dex underabundant in all neutron-capture elements, thus indicating a different birth environment.

Recently, the $[\text{EuII}/\alpha]$ ratio has been proposed as a strong discriminant between accreted and in situ GCs due to its effectiveness in tracing different timescales of star formation (Monty et al. 2024, Ou et al. 2024). As shown in the top panel of Figure

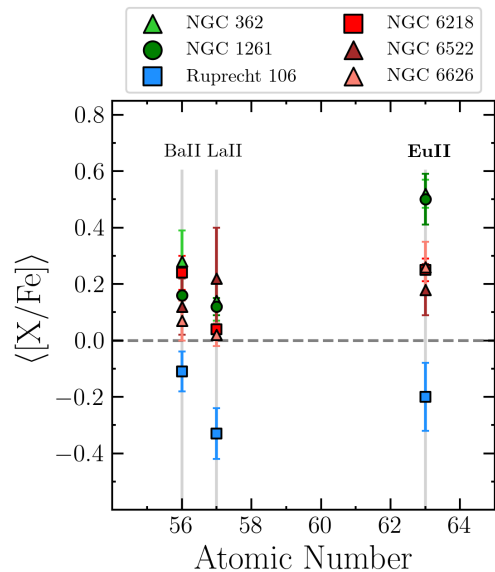


Fig. 5. Comparison of mean abundance ratios of the neutron-capture elements $[\text{BaII}/\text{Fe}]$, $[\text{LaII}/\text{Fe}]$, and $[\text{EuII}/\text{Fe}]$ for target GCs. The color coding is the same as in Figure 3. Errorbars indicate the standard deviation.

6, the two GSE GCs follow the expected behaviour compared to NGC 6218, NGC 6522 and NGC 6626, while we do not find sign of a consistent enhancement in $[\text{EuII}/\alpha]$ for Rup106. Thus, we recommend caution when using this diagnostic, as it might be effective for individual progenitors like GSE, but not in general for birth environments spanning a wide range of formation and evolutionary properties. Moreover, as demonstrated by the $[\text{EuII}/\text{BaII}]$ and the $[\text{EuII}/\text{LaII}]$ ratios (see bottom panel of Figure 6), in situ GCs and Rup106 show signs of higher efficiency in the production of heavy s -process elements with respect to the r -process elements when compared to the GSE GCs. We highlight that accreted systems considered here can be either r -process dominated (GSE) or s -process dominated (Rup106). Moreover, we find a difference of ≥ 0.2 dex in $[\text{EuII}/\text{YII}]$ between the three accreted cluster and the three in situ systems. Interestingly, the $[\text{EuII}/\text{YII}]$ ratio is similar in all accreted systems, regardless of the r - s - process dominance. This comparison may suggest that the applicability of $[\text{EuII}/\text{YII}]$ as a tracer of the accreted/in situ origin is more general than $[\text{EuII}/\text{BaII}]$ and $[\text{EuII}/\text{LaII}]$. Thus, this abundance ratio can play an important role in discriminating between in situ and accreted GCs at this metallicity, but, as for Zn, we point out that this diagnostic might lack sensitivity to discriminate between independent accreted progenitors.

5. Comparison with field stars from the likely progenitor system

In this section, we investigate the compatibility of the abundances derived in accreted GCs with those of field stars associated to their respective progenitors, and in passing we remark once again that homogeneity in this kind of comparison is crucial. In fact, several factors may contribute to a zero-point offset in abundance between our results and those from the literature. Discrepancies in the assumed atmospheric parameters, model at-

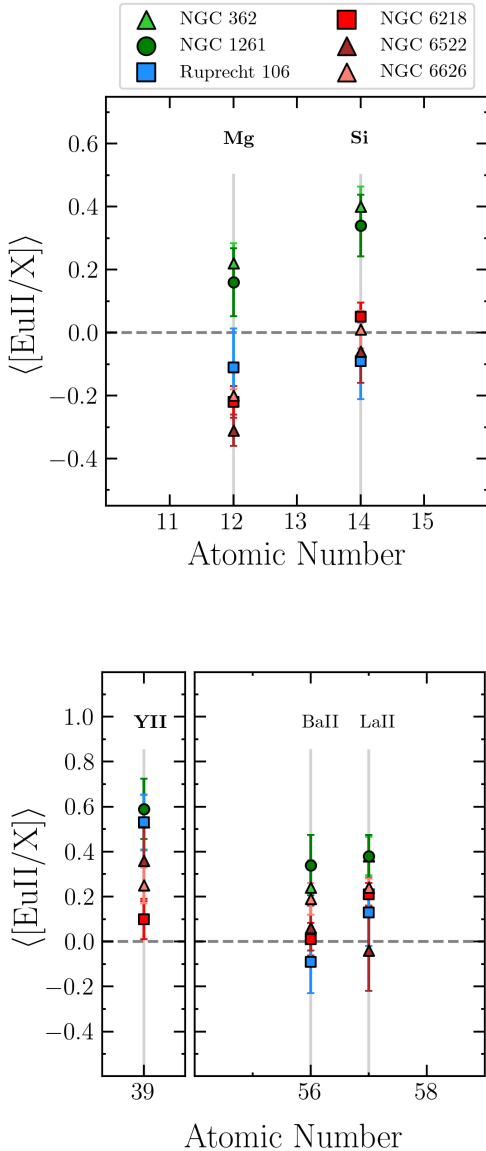


Fig. 6. Comparison of mean abundance ratios of EuII relative to other chemical elements for target GCs. The color coding is the same as in Figure 3. Errorbars indicate the standard deviation.

mosphere, solar mixture, linelist, and atomic data (e.g., $\log gf$) can potentially result in variations in the derived abundances.

5.1. NGC 6218, NGC 6522, NGC 6626 and the Milky Way

We use as a comparison the results obtained from high resolution spectroscopy of MW field stars, focusing on the chemical elements that show significant differences in accreted and in situ GCs. To do so, given the extremely high-quality of their stellar spectra, we selected the catalogue by Nissen & Schuster (2010, 2011) as our benchmark comparison dataset, and in particular we focused on stars in the high- α sequence that have been observed with UVES at VLT. To maintain homogeneity in the chemical analysis, we re-derived abundances from spectra of these stars (see details of the method in Section 3). The only exception in this homogeneous comparison is the element EuII, as (i) the number of available spectra in the literature is limited (and many

of them were obtained with different instruments and S/N), and (ii) abundances are derived from different spectral lines, due to the different evolutionary stages of the observed stars. We choose to compare our results with EuII abundances from the high- α sequence of Fishlock et al. (2017).

In Figure 7 we show that the abundances of NGC 6218, NGC 6522, and NGC 6626 match that of field stars (gray filled points) in all chemical spaces of interest (i.e., Ca, TiI, Zn, YII and EuII) except for Mg, where the three in situ target GCs show enhancement in $[Mg/Fe]$ compared to MW high- α sequence stars, being outside the 2σ of their distribution in the metallicity range of $-1.3 \leq [Fe/H] \leq -1.0$ dex.

5.2. NGC 362, NGC 1261 and Gaia-Sausage-Enceladus

The reference catalogue used for this comparison is the one by Ceccarelli et al. (2024), which has been produced with the same methods described here. Additionally, we re-derived the abundances for the stars in the low- α sequence of Nissen & Schuster (2010). Finally, we compared our abundances with the results from the low- α stars in Fishlock et al. (2017), Aguado et al. (2021), Carrillo et al. (2022), Giribaldi & Smiljanic (2023) and François et al. (2024) for EuII. As displayed in Figure 8, there is excellent agreement between the chemical composition of NGC 362 and NGC 1261 and the patterns shown by GSE stars (gray filled points) in the α -elements Ca and TiI, while, as for in situ GCs, the two GCs lay in the upper boundaries (at the 1.3σ and 1.6σ levels for NGC 362 and NGC 1261, respectively) of the distribution of GSE field stars in $[Mg/Fe]$ in the metallicity range of interest. The value of $[Zn/Fe]$ derived in NGC 1261 is consistent with those observed in the most Zn-poor stars in GSE, while NGC 362 seems to be slightly depleted (~ 0.1 dex) compared to them. Finally, the slightly subsolar values of $[YII/Fe]$ are consistent with those observed in literature (Aguado et al. 2021, Ceccarelli et al. 2024, François et al. 2024), as well as the high $[EuII/Fe]$ ratios (see also, Aguado et al. 2021, Matsuno et al. 2021, François et al. 2024, Ou et al. 2024).

This comparison represents strong additional evidence that the two selected GCs were indeed born in the GSE dwarf galaxy, and provides important confirmation that GCs and stars trace the same chemical evolution when sharing the birth environment (see also Monty et al. 2024).

5.3. Ruprecht 106 and the Helmi Streams

In this Section we investigate the compatibility of the chemical composition of Rup106 and that of stars formed in the galaxy that originated the Helmi Streams (Helmi et al. 1999), as a tentative dynamical connection between the two has been pointed out by several works (Massari et al. 2019, Forbes 2020, Callingham et al. 2022). In Figure 9, we present the mean abundances of Rup106 derived in this work (blue filled squares) compared to the high-resolution abundances of 11 stars linked to the Helmi Streams (grey filled points, Matsuno et al. 2022a, M22 hereafter). Note that we cannot compare Eu abundances as they were not published in M22, and we thus show Ni as an additional comparison, representative of the iron-peak group. To ensure homogeneity in the comparison, we re-analyze the spectra of the Helmi Streams stars following the procedure described in Section 3. The results are shown in Figure 9 (black filled points). The average offset between our and M22 abundances is consistent with zero for all the elements we show in Figure 9, except for TiI, Ni and YII, for which we find mild

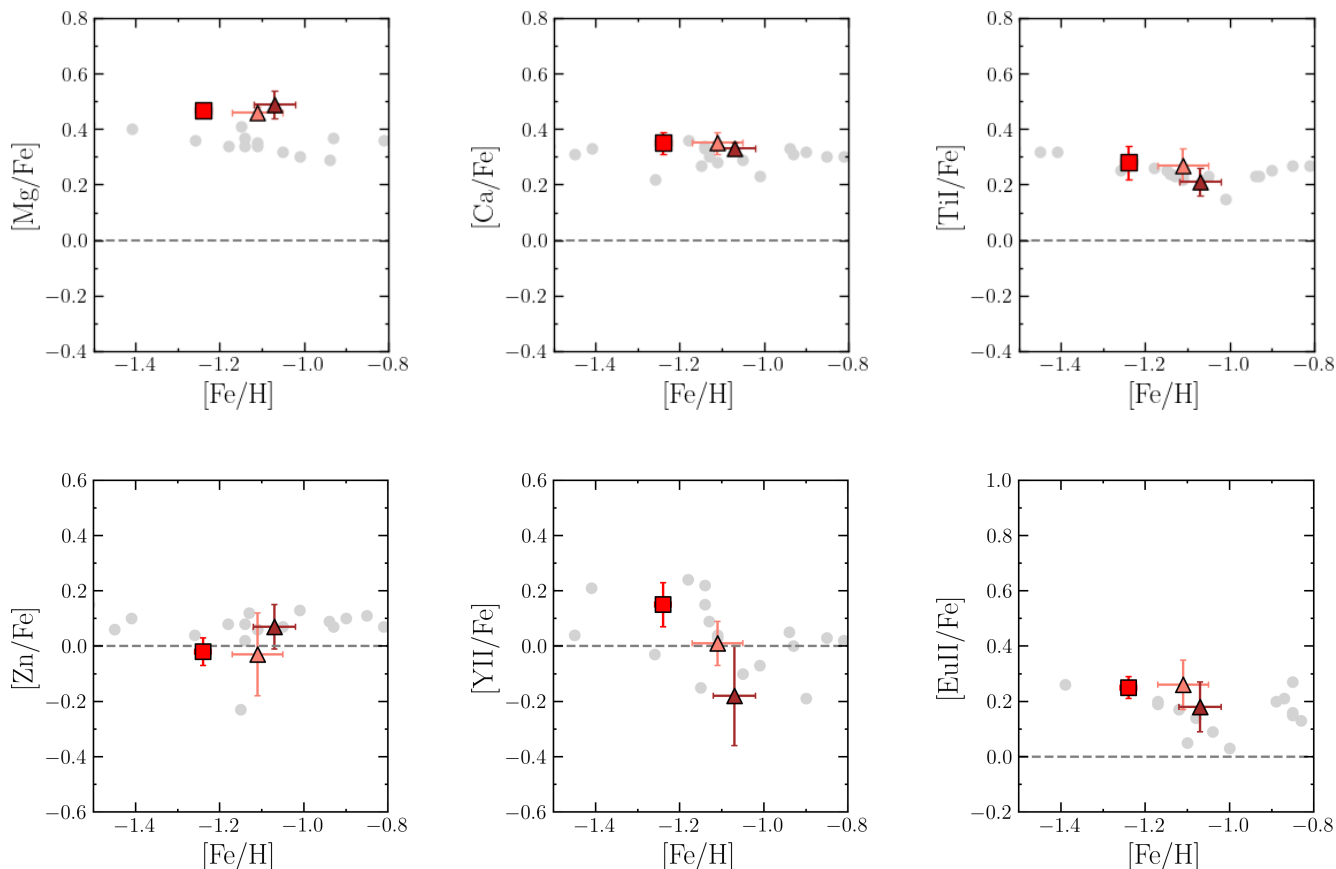


Fig. 7. Mean abundances of NGC 6218, NGC 6522 and NGC 6626 derived in this work (the color coding is the same as in Figure 3) compared with those derived for MW stars (gray filled points). [EuII/Fe] literature abundances are taken from [Fishlock et al. \(2017\)](#). Errorbars stand for the standard deviation.

offsets of +0.08 dex ($\sigma = 0.04$), of -0.08 dex ($\sigma = 0.05$), and of +0.09 dex ($\sigma = 0.07$), respectively. Regardless of the adopted data set (even though the most homogeneous comparison is the one with our re-analysed abundances), when comparing the mean abundance ratios of Rup106 to the trend observed in the Helmi Streams, a noticeable difference emerges, particularly in the α -elements. Our findings consistently indicate $[\alpha/\text{Fe}]$ values approximately 0.2 dex lower in comparison to the Helmi Streams, hinting at a lower star formation efficiency in the environment where Rup106 formed. Among the other elements studied, the most significant differences arise in Ni and YII with Rup106 being depleted by ~ 0.2 dex and by ~ 0.4 dex respectively. Therefore, in order to account for the observed differences shown in Figure 9, the progenitor of the Helmi Streams should have been massive enough to be chemically inhomogeneous. Otherwise, this chemical incongruity is a strong evidence supporting the interpretation that Rup106 was born in a different environment compared to the progenitor of the Helmi Streams.

6. On the possible origin of Ruprecht 106

In light of the chemical difference between Rup106 and the Helmi Streams stars, as well as because of its peculiar chemical composition compared to many other GCs (e.g., [Brown et al. 1997](#), [Carretta et al. 2009, 2013](#), [Villanova et al. 2013](#), [Monaco et al. 2018](#), [Puls et al. 2018](#), [Crestani et al. 2019](#), [Masseron et al. 2019](#), [Horta et al. 2020](#), [Mucciarelli et al. 2021b](#)), the birth envi-

ronment of Rup106 likely underwent a unique chemical evolution. In the following we discuss some possible interpretations.

6.1. Comparison with NGC 121

Given its extremely peculiar chemical composition, Rup106 has long been regarded as originating in an extragalactic environment. Initially, several work proposed it to be accreted from the Magellanic Clouds ([Lin & Richer 1992](#), [Fusi Pecci et al. 1995](#)), and particularly from the Small Magellanic Cloud (SMC). Even though recent post-*Gaia* kinematics studies of the orbit in the MW of Rup106 (see Section 1) have excluded the possibility of it originating in the SMC, it is interesting to note that Rup106 is coeval with NGC 121, the oldest SMC globular cluster (~ 10.5 Gyr, [Glatt et al. 2008](#), [Forbes & Bridges 2010](#), [Dotter et al. 2011](#)) and shows very similar metallicity ([Dalessandro et al. 2016](#), [Mucciarelli et al. 2023](#)). Therefore, this presents an excellent opportunity to explore the possibility of having an SMC-like galaxy as progenitor of Rup106. We will directly compare our results with [Mucciarelli et al. \(2023\)](#), given the congruent analytical approaches. As shown in Figure 10, NGC 121 (yellow filled squares) has solar-scaled $[\alpha/\text{Fe}]$, hinting at an enrichment due to SN Ia already in place in the SMC ~ 10.5 Gyr ago. These values are, on average, 0.1 - 0.2 dex α -enriched relative to what we find for Rup106, suggesting that Rup106 likely formed in an environment with an even less efficient star formation compared to the SMC. Regarding the iron-peak elements, we find compa-

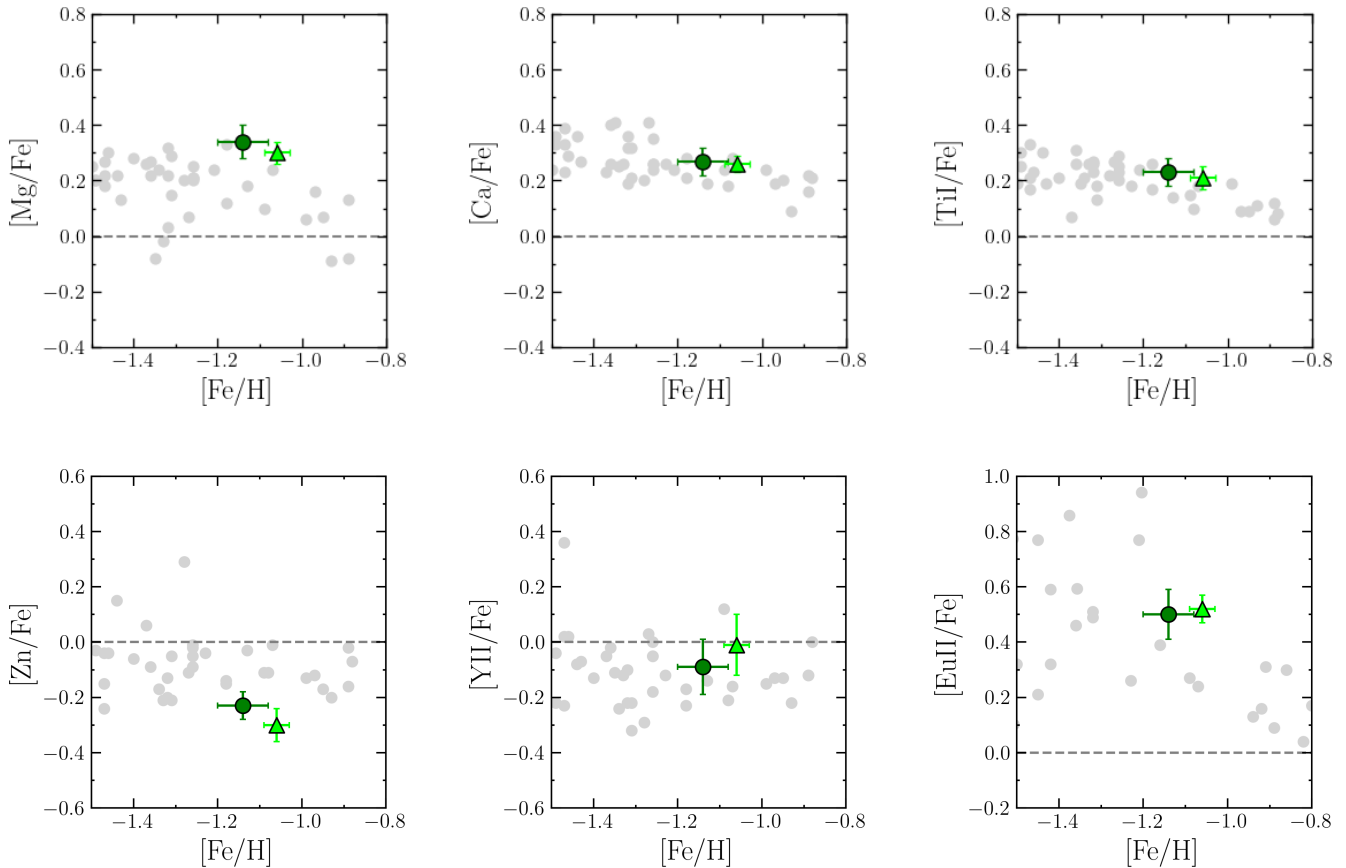


Fig. 8. Mean abundances of NGC 362 and NGC 1261 derived in this work (the color coding is the same as in Figure 3) compared with those of GSE stars (gray filled points, either derived in this work and by Ceccarelli et al. (2024) for Mg, Ca, Ti, Zn and YII). Literature abundances for [EuII/Fe] have been taken from Fishlock et al. (2017), Aguado et al. (2021), Carrillo et al. (2022), Giribaldi & Smiljanic (2023), François et al. (2024). Errorbars stand for the standard deviation.

rable values in the abundances ratios of Cu. The very low values of [Cu/Fe] found in both Rup106 and NGC 121 are consistent with those of the SMC field stars (Mucciarelli et al. 2023) and 0.5 dex underabundant compared to MW GCs and stars, favouring a chemical enrichment scenario in which the contribution by massive stars is extremely reduced, as also discussed in Section 4.2. Additionally, Rup106 shows lower abundances (~ 0.2 dex) of other elements produced in massive stars (i.e., Sc, V, and Co) relative to NGC 121 and also in Ni. Interestingly, the only elements in which enhancement is detected in Rup106 are Cr and Mn. These elements are predominantly synthesized by SN Ia, with yields depending on the metallicity of the progenitor SN Ia. Unfortunately, Mucciarelli et al. (2023) do not provide an estimate of [Zn/Fe] for NGC 121. When assessing s -process elements, we note similar Ba abundances between the two clusters, yet discern distinct values in Y and La, with Rup106 being, once again, depleted in these elements. Given that NGC 121 demonstrates pronounced deficiencies in these elements relative to the only other SMC GC of similar age, this discrepancy highlights the unique conditions under which Rup106 formed. Also, the efficiency of production of r -process element is extremely low, with Rup106 being ~ 0.7 dex underabundant in Eu relative to NGC 121, which conversely aligns with observations in GSE GCs and SMC stars. This comparison further underlines that Rup106 originated in an environment that was significantly different to the SMC of 10.5 Gyr ago, probably characterized by

an exceptionally low star formation efficiency and likely featured a truncated initial mass function (IMF) with minimal contribution from massive stars.

6.2. Comparison with surviving dwarf galaxies

A similar chemical composition to that of Rup106 has been observed in stars belonging to dwarf galaxies in the Local Group (Venn et al. 2004, Tolstoy et al. 2009). Indeed, subsolar $[\alpha/\text{Fe}]$ values at $[\text{Fe}/\text{H}] \leq -1.5$ dex are observed in surviving dwarf galaxies like Carina, Fornax, Sculptor, Sextans, and Ursa Minor (Venn et al. 2012, Hendricks et al. 2014, Hill et al. 2019, Theler et al. 2020, Fernandes et al. 2023, Sestito et al. 2023). The low values of Zn ($[\text{Zn}/\text{Fe}] \sim -0.3$ dex) compared to MW stars, as derived for Rup106, are also typical these systems (see Fig. 16 of Skúladóttir et al. 2017, and reference therein). Finally, most of the dwarf galaxies show enhancement in [EuII/Fe] compared to MW stars due to either the very low star formation efficiency and the delayed contribution to the production of Eu by NSMs (Letarte et al. 2010, Venn et al. 2012, Lemasle et al. 2014). However, even the extremely low [EuII/Fe] of Rup106 can be reproduced in some of these systems, like, e.g., Sculptor (Hill et al. 2019). Indeed, these authors find several stars in Sculptor with subsolar values (~ -0.1 dex) of [EuII/BaII] at $[\text{Fe}/\text{H}] \sim -1.3$ dex, suggesting that the onset of s -process enrichment was already in place at this metallicity. It is interesting

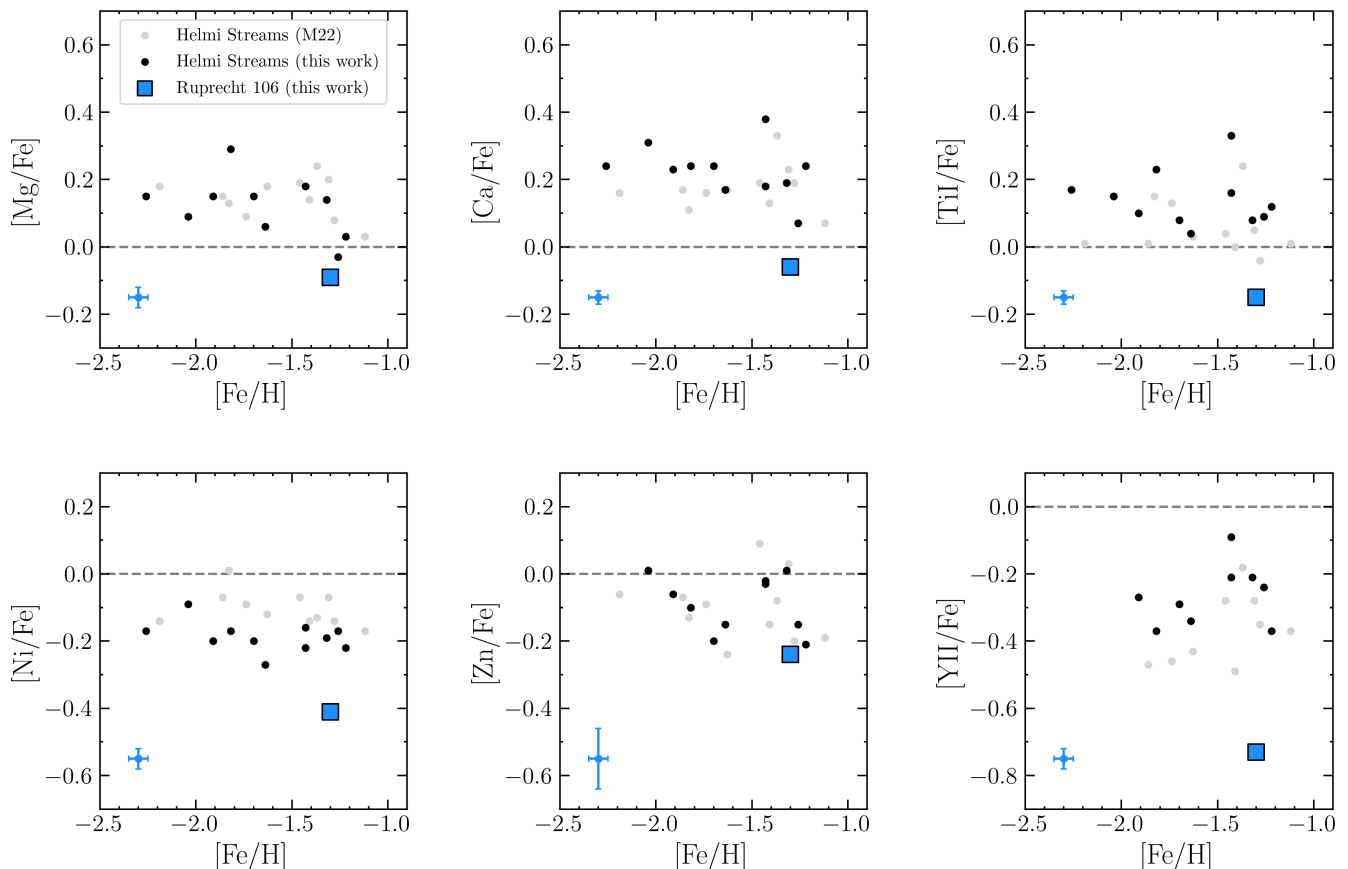


Fig. 9. Mean abundances of Rup106 derived in this work (blue filled squares) compared with those derived for field stars associated with the Helmi Streams (results from this work and from M22 are shown in black and grey, respectively). In the bottom left corner we plot the standard deviation.

to note that the chemical composition of Rup106 recalls that of iron-rich metal-poor stars (IRMP), despite they being unlikely to form in GCs, thus indicating a birth environment enriched by the (double) detonation of sub-Chandrasekhar-mass CO white dwarfs (Reggiani et al. 2023). This further support the idea that Rup106 formed in a dwarf galaxy, as these authors demonstrated that IRMP stars are easier to find in surviving dwarf galaxies and the Magellanic Clouds, rather than in the halo of the MW.

It is important to note that the majority of the existing systems that reproduce the peculiar chemistry of Rup106 have a stellar mass ($\sim 10^6 M_{\odot}$, McConnachie 2012) that is not compatible with the one that has been estimated for the progenitor of the Helmi Streams, with the latter being roughly 100 times more massive (Koppelman et al. 2019). Therefore, if the dynamical association of Rup106 is accurate, the possibility that it did not form directly in the progenitor of the Helmi Streams cannot be ruled out. We speculate that Rup106 could have formed in a dwarf galaxy with a mass comparable to that of Sculptor, that, based on Rup106 dynamical properties, could have been a satellite of the progenitor of the Helmi Streams or the Sagittarius dwarf (Davies et al. 2024), on a similar note to the case of the GC NGC 2005 in the Large Magellanic Cloud (Mucciarelli et al. 2021b).

7. Conclusion

The primary aim of this work is to discern potential distinctions in elemental abundances among four GCs of very similar metal-

licity that are expected to have formed in different environments, and to understand which elements are most sensitive to their different origin.

The outcome of this homogeneous chemical analysis reveals striking similarities in the chemical abundances of NGC 362 and NGC 1261, two GCs that were accreted during the merging event with the *Gaia*-Sausage-Enceladus dwarf galaxy. When comparing their abundances with those from the in situ GCs NGC 6218, NGC 6522 and NGC 6626, a coherent and distinct overall pattern emerges in the α -elements, especially in Mg, Si, and Ca, where we identify an depletion of ~ 0.1 dex in the GSE GCs with respect to in situ GCs. This finding agrees with observations of Halo field stars, where distinctions between in-situ and accreted stars, especially in the α -elements, are discernible around this values of [Fe/H], whereas chemical patterns become indistinguishable at lower metallicity (Horta et al. 2023, Ceccarelli et al. 2024). This is consistent with the fact that it took 2 Gyr less to NGC 6218, NGC 6522 and NGC 6626 to reach the same metallicity as the GSE GCs (Dotter et al. 2010, 2011, VandenBerg et al. 2013, Villanova et al. 2017, Kerber et al. 2018), indicating that the contribution of SN Ia to the chemical enrichment of the gas was not in place at the time when this system formed. Moreover, statistically significant variations are observed in specific elements such as Zn and Eu, whose production sites are directly associated with massive stars (HNe for Zn and rCCSNe+NSMs for Eu). It is noteworthy to emphasize that these events are inherently rare, thus they might exert a profound influence on the abundances within a given environment. These results reinforce

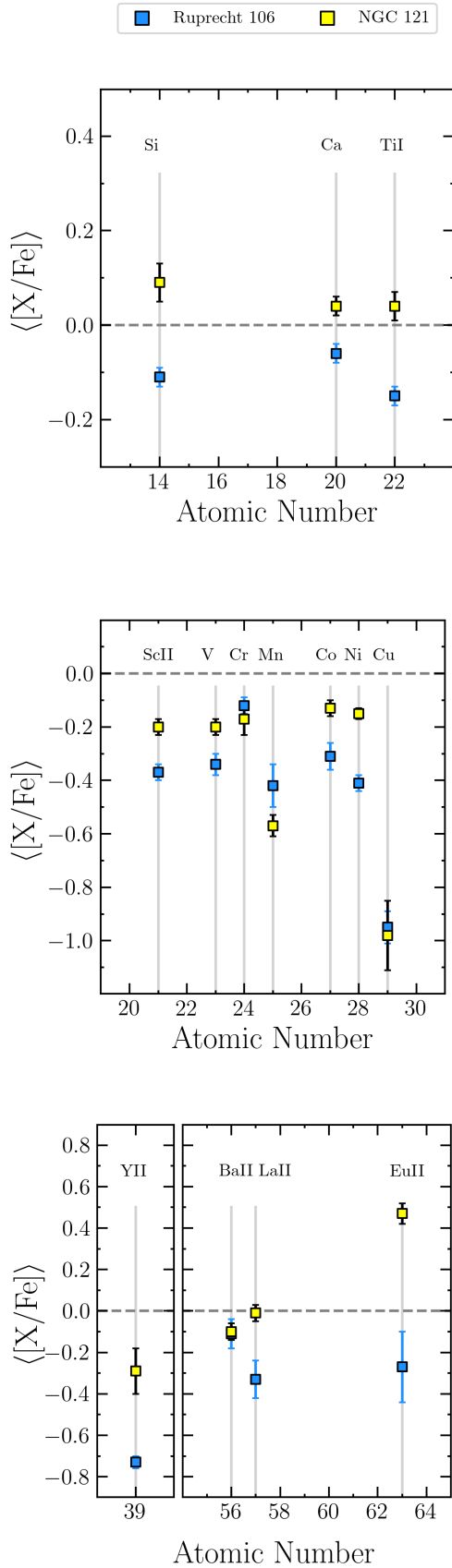


Fig. 10. Mean abundances of the α - (top panel), iron-peak (middle panel) and neutron-capture (bottom panel) elements in Rup106 (blue filled squares) and NGC 121 (yellow filled triangles). Errorbars indicate the standard deviation.

the idea that chemical tagging is an effective tool to investigate the origin of GCs, even when comparing chemical composition of GCs formed in different progenitor, but at the same time warn that not every element is equally sensitive in this sense.

In this coherent picture, Rup106 stands out as a very distinct character. Indeed, Rup106 follows the AMR of accreted GCs (Forbes & Bridges 2010, Dotter et al. 2010, 2011, Vandenberg et al. 2013), whereas MW in situ clusters of similar age clearly experienced a different chemical enrichment path, exhibiting significantly higher metallicity (0.5 - 0.8 dex more metal rich, Massari et al. 2023). Despite the congruence between Rup106 and the GSE GCs in the age-metallicity space, differences emerge when examining all their chemical elements. Particularly, Rup106 exhibits subsolar $[\alpha/Fe]$ values, that are typical of an environment already enriched by SNe Ia, in contrast to GSE clusters ($[\alpha/Fe] > 0.3$ dex), where SNe Ia have only just started contributing to the pollution of the gas. This comparison underlines distinct chemical evolution histories between GSE and the environment in which Rup106 formed, with the latter experiencing slower and less efficient star formation and, likely, an IMF truncated of most of the massive stars, indicating a lower mass for the host of Rup106 at ~ 10.5 Gyr ago compared to GSE.

In light of these results, this work demonstrates that the exceptionally high precision offered by a strictly homogeneous chemical analysis allows chemical tagging to play a crucial role in uncovering the true origin of GCs. Particularly, this method enables to clearly discriminate not only between GCs formed within the MW and those formed in other accreted galaxies, but also to distinguish the chemical signatures of GCs originating from independent accreted progenitors.

Finally, we interpret the extreme peculiarity of the chemistry of Rup106 as due to a particular evolution of its progenitor, possibly the galaxy originating the Helmi Streams. However, the remarkably low values in the $[\alpha/Fe]$ abundance ratios, as well as some other heavier elements, compared to Helmi Streams stars lend weight to the possibility that Rup106 originated from an even smaller galaxy, with a stellar mass comparable to that of some surviving dwarf galaxies (e.g., Sculptor).

Acknowledgements. Based on observations collected at the ESO-VLT under the programs 069.D-0227 (P.I. P. François), 073.D-0211 (P.I. E. Carretta), 083.D-0208 (P.I. E. Carretta), 097.D-0175 (P.I. B. Barbuy), 091.D-0535 (P.I. C. Moni Bidin), 0101.D-0109 (P.I. A. Marino), 193.D-0232 (P.I. F. R. Ferraro), and 197.B-1074 (P.I. G. F. Gilmore). This research is funded by the project *LEGO – Reconstructing the building blocks of the Galaxy by chemical tagging* (P.I. A. Mucciarelli), granted by the Italian MUR through contract PRIN 2022LLP8TK_001. MB, EC, AM and DM acknowledge the support to this study by the PRIN INAF 2023 grant ObFu *CHAM - Chemodynamics of the Accreted Halo of the Milky Way* (P.I. M. Bellazzini). DM acknowledges financial support from PRIN-MIUR-22 “CHRONOS: adjusting the clock(s) to unveil the CHRONO-chemo-dynamical Structure of the Galaxy” (P.I. S. Cassisi) granted by the European Union - Next Generation EU. DM and MB acknowledge the support to activities related to the ESA/*Gaia* mission by the Italian Space Agency (ASI) through contract 2018-24-HH.0 and its addendum 2018-24-HH.1-2022 to the National Institute for Astrophysics (INAF). We thank the anonymous referee for the helpful comments that improved the quality of the paper. This work has made use of data from the European Space Agency (ESA) mission *Gaia* <https://www.cosmos.esa.int/gaia>), processed by the *Gaia* Data Processing and Analysis Consortium (DPAC, <https://www.cosmos.esa.int/web/gaia/dpac/consortium>). Funding for the DPAC has been provided by national institutions, in particular the institutions participating in the *Gaia* Multilateral Agreement. This work made use of SDSS-IV data. Funding for the Sloan Digital Sky Survey IV has been provided by the Alfred P. Sloan Foundation, the U.S. Department of Energy Office of Science, and the Participating Institutions. SDSS-IV acknowledges support and resources from the Center for High Performance Computing at the University of Utah. The SDSS website is www.sdss4.org. SDSS-IV is managed by the Astrophysical Research Consortium for the Participating Institutions of the SDSS Collaboration including the Brazilian Participation Group, the Carnegie Institution for Sci-

ence, Carnegie Mellon University, Center for Astrophysics | Harvard & Smithsonian, the Chilean Participation Group, the French Participation Group, Instituto de Astrofísica de Canarias, The Johns Hopkins University, Kavli Institute for the Physics and Mathematics of the Universe (IPMU) / University of Tokyo, the Korean Participation Group, Lawrence Berkeley National Laboratory, Leibniz Institut für Astrophysik Potsdam (AIP), Max-Planck-Institut für Astronomie (MPIA Heidelberg), Max-Planck-Institut für Astrophysik (MPA Garching), Max-Planck-Institut für Extraterrestrische Physik (MPE), National Astronomical Observatories of China, New Mexico State University, New York University, University of Notre Dame, Observatório Nacional / MCTI, The Ohio State University, Pennsylvania State University, Shanghai Astronomical Observatory, United Kingdom Participation Group, Universidad Nacional Autónoma de México, University of Arizona, University of Colorado Boulder, University of Oxford, University of Portsmouth, University of Utah, University of Virginia, University of Washington, University of Wisconsin, Vanderbilt University, and Yale University.

References

- Abdurro'uf, Accetta, K., Aerts, C., et al. 2022, *ApJS*, 259, 35
- Aguado, D. S., Belokurov, V., Myeong, G. C., et al. 2021, *ApJ*, 908, L8
- Alvarez Garay, D. A., Mucciarelli, A., Bellazzini, M., Lardo, C., & Ventura, P. 2024, *A&A*, 681, A54
- Amarante, J. A. S., Debattista, V. P., Beraldo e Silva, L., Laporte, C. F. P., & Deg, N. 2022, *ApJ*, 937, 12
- Andrae, R., Fouesneau, M., Creevey, O., et al. 2018, *A&A*, 616, A8
- Barbuy, B., Cantelli, E., Muniz, L., et al. 2021, *A&A*, 654, A29
- Bastian, N. & Lardo, C. 2018, *ARA&A*, 56, 83
- Baumgardt, H. & Vasiliev, E. 2021, *MNRAS*, 505, 5957
- Bellazzini, M., Ibata, R., Malhan, K., et al. 2020, *A&A*, 636, A107
- Belokurov, V., Erkal, D., Evans, N. W., Koposov, S. E., & Deason, A. J. 2018, *MNRAS*, 478, 611
- Belokurov, V. & Kravtsov, A. 2022, *MNRAS*, 514, 689
- Belokurov, V. & Kravtsov, A. 2024, *MNRAS*, 528, 3198
- Belokurov, V., Vasiliev, E., Deason, A. J., et al. 2023, *MNRAS*, 518, 6200
- Brodie, J. P. & Strader, J. 2006, *ARA&A*, 44, 193
- Brown, J. A., Wallerstein, G., & Zucker, D. 1997, *AJ*, 114, 180
- Callingham, T. M., Cautun, M., Deason, A. J., et al. 2022, *MNRAS*, 513, 4107
- Cardelli, J. A., Clayton, G. C., & Mathis, J. S. 1989, *ApJ*, 345, 245
- Carretta, E., Bragaglia, A., Gratton, R., & Lucatello, S. 2009, *A&A*, 505, 139
- Carretta, E., Bragaglia, A., Gratton, R., et al. 2010, *ApJ*, 712, L21
- Carretta, E., Bragaglia, A., Gratton, R. G., et al. 2013, *A&A*, 557, A138
- Carrillo, A., Hawkins, K., Jofré, P., et al. 2022, *MNRAS*, 513, 1557
- Castelli, F. & Kurucz, R. L. 2003, in *Modelling of Stellar Atmospheres*, ed. N. Piskunov, W. W. Weiss, & D. F. Gray, Vol. 210, A20
- Ceccarelli, E., Massari, D., Mucciarelli, A., et al. 2024, *A&A*, 684, A37
- Cescutti, G., Romano, D., Matteucci, F., Chiappini, C., & Hirschi, R. 2015, *A&A*, 577, A139
- Chen, Y. & Gnedin, O. Y. 2024, *The Open Journal of Astrophysics*, 7, 23
- Crestani, J., Alves-Brito, A., Bono, G., Puls, A. A., & Alonso-García, J. 2019, *MNRAS*, 487, 5463
- Dalessandro, E., Lapenna, E., Mucciarelli, A., et al. 2016, *ApJ*, 829, 77
- Davies, E. Y., Monty, S., Belokurov, V., & Dillamore, A. M. 2024, *MNRAS*, 529, 772
- Dekker, H., D'Odorico, S., Kaufer, A., Delabre, B., & Kotzłowski, H. 2000, in *Society of Photo-Optical Instrumentation Engineers (SPIE) Conference Series*, Vol. 4008, *Optical and IR Telescope Instrumentation and Detectors*, ed. M. Iye & A. F. Moorwood, 534–545
- Dell'Agli, F., García-Hernández, D. A., Ventura, P., et al. 2018, *MNRAS*, 475, 3098
- Dotter, A., Milone, A. P., Conroy, C., Marino, A. F., & Sarajedini, A. 2018, *ApJ*, 865, L10
- Dotter, A., Sarajedini, A., & Anderson, J. 2011, *ApJ*, 738, 74
- Dotter, A., Sarajedini, A., Anderson, J., et al. 2010, *ApJ*, 708, 698
- Fernandes, L., Mason, A. C., Horta, D., et al. 2023, *MNRAS*, 519, 3611
- Fishlock, C. K., Yong, D., Karakas, A. I., et al. 2017, *MNRAS*, 466, 4672
- Forbes, D. A. 2020, *MNRAS*, 493, 847
- Forbes, D. A. & Bridges, T. 2010, *MNRAS*, 404, 1203
- François, P., Cescutti, G., Bonifacio, P., et al. 2024, *arXiv e-prints*, arXiv:2404.08418
- Freljij, H., Villanova, S., Muñoz, C., & Fernández-Trincado, J. G. 2021, *MNRAS*, 503, 867
- Fusi Pecci, F., Bellazzini, M., Cacciari, C., & Ferraro, F. R. 1995, *AJ*, 110, 1664
- Gaia Collaboration, Babusiaux, C., van Leeuwen, F., et al. 2018, *A&A*, 616, A10
- Gaia Collaboration, Brown, A. G. A., Vallenari, A., et al. 2021, *A&A*, 649, A1
- Gaia Collaboration, Vallenari, A., Brown, A. G. A., et al. 2023, *A&A*, 674, A1
- Giribaldi, R. E. & Smiljanic, R. 2023, *A&A*, 673, A18
- Glatt, K., Gallagher, John S., I., Grebel, E. K., et al. 2008, *AJ*, 135, 1106
- Grevesse, N. & Sauval, A. J. 1998, *Space Sci. Rev.*, 85, 161
- Harris, W. E. 2010, *arXiv e-prints*, arXiv:1012.3224
- Helmi, A. 2020, *ARA&A*, 58, 205
- Helmi, A., Babusiaux, C., Koppelman, H. H., et al. 2018, *Nature*, 563, 85
- Helmi, A. & de Zeeuw, P. T. 2000, *MNRAS*, 319, 657
- Helmi, A., White, S. D. M., de Zeeuw, P. T., & Zhao, H. 1999, *Nature*, 402, 53
- Hendricks, B., Koch, A., Walker, M., et al. 2014, *A&A*, 572, A82
- Hill, V., Skúladóttir, Á., Tolstoy, E., et al. 2019, *A&A*, 626, A15
- Horta, D., Schiavon, R. P., Mackereth, J. T., et al. 2020, *MNRAS*, 493, 3363
- Horta, D., Schiavon, R. P., Mackereth, J. T., et al. 2023, *MNRAS*, 520, 5671
- Ibata, R., Malhan, K., Tenachi, W., et al. 2024, *ApJ*, 967, 89
- Ibata, R. A., Gilmore, G., & Irwin, M. J. 1994, *Nature*, 370, 194
- Kerber, L. O., Nardiello, D., Ortolani, S., et al. 2018, *ApJ*, 853, 15
- Kobayashi, C., Karakas, A. I., & Lugaro, M. 2020, *ApJ*, 900, 179
- Kobayashi, C. & Nomoto, K. 2009, *ApJ*, 707, 1466
- Koch-Hansen, A. J., Hansen, C. J., & McWilliam, A. 2021, *A&A*, 653, A2
- Koppelman, H. H., Helmi, A., Massari, D., Price-Whelan, A. M., & Starkenburg, T. K. 2019, *A&A*, 631, L9
- Kruijssen, J. M. D., Pfeffer, J. L., Reina-Campos, M., Crain, R. A., & Bastian, N. 2019, *MNRAS*, 486, 3180
- Kurucz, R. L. 2005, *Memorie della Societa Astronomica Italiana Supplementi*, 8, 14
- Lagioia, E. P., Milone, A. P., Legnardi, M. V., et al. 2024, *arXiv e-prints*, arXiv:2406.16824
- Lattimer, J. M. & Schramm, D. N. 1974, *ApJ*, 192, L145
- Leaman, R., VandenBerg, D. A., & Mendel, J. T. 2013, *MNRAS*, 436, 122
- Lemasle, B., de Boer, T. J. L., Hill, V., et al. 2014, *A&A*, 572, A88
- Letarte, B., Hill, V., Tolstoy, E., et al. 2010, *A&A*, 523, A17
- Limberg, G., Souza, S. O., Pérez-Villegas, A., et al. 2022, *ApJ*, 935, 109
- Lin, D. N. C. & Richer, H. B. 1992, *ApJ*, 388, L57
- Lucertini, F., Monaco, L., Caffau, E., et al. 2023, *A&A*, 671, A137
- Majewski, S. R., Skrutskie, M. F., Weinberg, M. D., & Osthheimer, J. C. 2003, *ApJ*, 599, 1082
- Malhan, K., Ibata, R. A., Sharma, S., et al. 2022, *ApJ*, 926, 107
- Marín-Franch, A., Aparicio, A., Piotto, G., et al. 2009, *ApJ*, 694, 1498
- Marino, A. F., Milone, A. P., Renzini, A., et al. 2021, *ApJ*, 923, 22
- Marino, A. F., Villanova, S., Piotto, G., et al. 2008, *A&A*, 490, 625
- Massari, D., Aguado-Agelet, F., Monelli, M., et al. 2023, *A&A*, 680, A20
- Massari, D., Koppelman, H. H., & Helmi, A. 2019, *A&A*, 630, L4
- Masseron, T., García-Hernández, D. A., Mészáros, S., et al. 2019, *A&A*, 622, A191
- Matsuno, T., Dodd, E., Koppelman, H. H., et al. 2022a, *A&A*, 665, A46
- Matsuno, T., Hirai, Y., Tarumi, Y., et al. 2021, *A&A*, 650, A110
- Matsuno, T., Koppelman, H. H., Helmi, A., et al. 2022b, *A&A*, 661, A103
- McConnachie, A. W. 2012, *AJ*, 144, 4
- Milone, A. P., Piotto, G., Bedin, L. R., et al. 2012, *A&A*, 540, A16
- Minelli, A., Mucciarelli, A., Massari, D., et al. 2021, *ApJ*, 918, L32
- Monaco, L., Villanova, S., Carraro, G., Mucciarelli, A., & Moni Bidin, C. 2018, *A&A*, 616, A181
- Monty, S., Belokurov, V., Sanders, J. L., et al. 2024, *arXiv e-prints*, arXiv:2405.08963
- Monty, S., Yong, D., Marino, A. F., et al. 2023a, *MNRAS*, 518, 965
- Monty, S., Yong, D., Massari, D., et al. 2023b, *MNRAS*, 522, 4404
- Moore, B., Ghigna, S., Governato, F., et al. 1999, *ApJ*, 524, L19
- Mösta, P., Roberts, L. F., Halevi, G., et al. 2018, *ApJ*, 864, 171
- Mucciarelli, A. 2013, *arXiv e-prints*, arXiv:1311.1403
- Mucciarelli, A., Bellazzini, M., & Massari, D. 2021a, *A&A*, 653, A90
- Mucciarelli, A., Massari, D., Minelli, A., et al. 2021b, *Nature Astronomy*, 5, 1247
- Mucciarelli, A., Minelli, A., Lardo, C., et al. 2023, *A&A*, 677, A61
- Mucciarelli, A., Pancino, E., Lovisi, L., Ferraro, F. R., & Lapenna, E. 2013, *ApJ*, 766, 78
- Myeong, G. C., Evans, N. W., Belokurov, V., Sanders, J. L., & Koposov, S. E. 2018, *ApJ*, 856, L26
- Myeong, G. C., Vasiliev, E., Iorio, G., Evans, N. W., & Belokurov, V. 2019, *MNRAS*, 488, 1235
- Naidu, R. P., Conroy, C., Bonaca, A., et al. 2022a, *arXiv e-prints*, arXiv:2204.09057
- Naidu, R. P., Ji, A. P., Conroy, C., et al. 2022b, *ApJ*, 926, L36
- Newton, O., Cautun, M., Jenkins, A., Frenk, C. S., & Helly, J. C. 2018, *MNRAS*, 479, 2853
- Nissen, P. E. & Schuster, W. J. 2010, *A&A*, 511, L10
- Nissen, P. E. & Schuster, W. J. 2011, *A&A*, 530, A15
- Ou, X., Ji, A. P., Frebel, A., Naidu, R. P., & Limberg, G. 2024, *arXiv e-prints*, arXiv:2404.10067
- Pagnini, G., Di Matteo, P., Khoperskov, S., et al. 2023, *A&A*, 673, A86
- Pasquini, L., Avila, G., Blecha, A., et al. 2002, *The Messenger*, 110, 1
- Peñarrubia, J., Walker, M. G., & Gilmore, G. 2009, *MNRAS*, 399, 1275
- Puls, A. A., Alves-Brito, A., Campos, F., Dias, B., & Barbuy, B. 2018, *MNRAS*, 476, 690

- Recio-Blanco, A. 2018, *A&A*, 620, A194
- Reggiani, H., Schlafman, K. C., & Casey, A. R. 2023, *AJ*, 166, 128
- Romano, D., Karakas, A. I., Tosi, M., & Matteucci, F. 2010, *A&A*, 522, A32
- Schiavon, R. P., Phillips, S. G., Myers, N., et al. 2024, *MNRAS*, 528, 1393
- Sestito, F., Zaremba, D., Venn, K. A., et al. 2023, *MNRAS*, 525, 2875
- Siegel, D. M., Barnes, J., & Metzger, B. D. 2019, *Nature*, 569, 241
- Skúladóttir, Á., Tolstoy, E., Salvadori, S., Hill, V., & Pettini, M. 2017, *A&A*, 606, A71
- Stetson, P. B. & Pancino, E. 2008, *PASP*, 120, 1332
- Theler, R., Jablonka, P., Lucchesi, R., et al. 2020, *A&A*, 642, A176
- Tolstoy, E., Hill, V., & Tosi, M. 2009, *ARA&A*, 47, 371
- Trujillo-Gomez, S., Kruijssen, J. M. D., Reina-Campos, M., et al. 2021, *MNRAS*, 503, 31
- Van der Swaelmen, M., Hill, V., Primas, F., & Cole, A. A. 2013, *A&A*, 560, A44
- VandenBerg, D. A., Brogaard, K., Leaman, R., & Casagrande, L. 2013, *ApJ*, 775, 134
- Vasiliev, E. & Baumgardt, H. 2021, *MNRAS*, 505, 5978
- Venn, K. A., Irwin, M., Shetrone, M. D., et al. 2004, *AJ*, 128, 1177
- Venn, K. A., Shetrone, M. D., Irwin, M. J., et al. 2012, *ApJ*, 751, 102
- Ventura, P., Di Criscienzo, M., Carini, R., & D'Antona, F. 2013, *MNRAS*, 431, 3642
- Villanova, S., Geisler, D., Carraro, G., Moni Bidin, C., & Muñoz, C. 2013, *ApJ*, 778, 186
- Villanova, S., Moni Bidin, C., Mauro, F., Muñoz, C., & Monaco, L. 2017, *MNRAS*, 464, 2730
- White, S. D. M. & Frenk, C. S. 1991, *ApJ*, 379, 52
- Yan, Z., Jerabkova, T., & Kroupa, P. 2020, *A&A*, 637, A68

Appendix A: Validation of the abundances

Appendix A.1: GSE globular clusters

To validate our findings, we undertake a comparative analysis with two distinct independent studies conducted on two of the six target GCs. Specifically, we compare our results to those obtained by the seminal works by Carretta et al. (2009, 2010, 2013) and to those provided by the latest data release of the APOGEE survey (Abdurro'uf et al. 2022). In particular, we use the APOGEE value-added catalogue of Galactic GC stars (Schivavon et al. 2024), limiting our comparison only to well-measured stars. To do so, we remove all the stars with the following flags³ in the quality parameters:

- ASPCAPFLAG = 16, 17, 23;
- STARFLAG = 3, 4, 9, 12, 13, 16;
- EXTRATARG = 4;
- VB_PROB > 0.99.

The choice of using these two dataset was guided by their execution of identical chemical analyses on two out of the four target GCs, thereby ensuring consistency in their outcomes. We limit our comparison with Carretta et al. (2009, 2010, 2013) and APOGEE only to the chemical elements identified as sensitive to the origin of GCs available in these dataset, that are Mg, Si and Ca. As shown in Figure A.1, the results from this work are in agreement within the uncertainties with those provided by Carretta et al. (2009, 2010, 2013) and APOGEE, consistently yielding an enhancement of 0.1 - 0.2 dex in the α -elements (Mg, Si, and Ca) of NGC 6218 with respect to NGC 362.

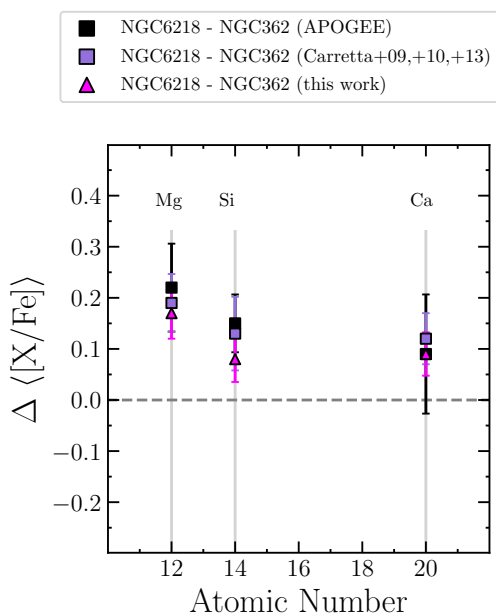


Fig. A.1. Difference of mean abundance ratios of the α -elements [Mg/Fe], [Si/Fe], and [Ca/Fe] between NGC 6218 and NGC 362 from this work (pink triangles), Carretta et al. (2009, 2010, 2013) (purple squares), and APOGEE (black squares). Errorbars indicate the standard deviation.

³ Flags definition available at <https://www.sdss4.org/dr17/irspec/apogee-bitmasks/>.

Appendix A.2: Comparison with V13

A comparison with the results of V13, who analyzed the same Rup106 dataset, further confirms the peculiarity of this system. Indeed, their findings indicate that, within this cluster, the observed spread in all chemical elements is consistent with the uncertainty on the measurement, suggesting Rup106 to be a single population GC, as also confirmed photometrically in more recent works (Dotter et al. 2018, Lagioia et al. 2024). Moreover, their analysis reveals solar-like abundances in the α -elements, alongside a notable underabundance in the iron peak elements relative to iron, ranging from 0.1 up to 0.8 dex. Firstly, when comparing the atmospheric parameters of Rup106 targets, we find a significant difference in the adopted T_{eff} scales, with an average discrepancy (this work – V13) of +169 K ($\sigma = 55$ K). The average difference for the surface gravity is +0.65 dex ($\sigma = 0.14$ dex) and that for v_t is -0.07 km/s ($\sigma = 0.05$ km/s). These discrepancies arise from the fact that V13 constrained T_{eff} and $\log g$ with a methodology similar to ours, deriving them from the photometry, but exploiting a different color - T_{eff} relation. On the other hand, V13 assumed a v_t derived from the relation by Marino et al. (2008), while we constrained it spectroscopically (see Section 3.1). To ensure a fair comparison between the results, we rescaled the abundance ratios reported in V13 on the Grevesse & Sauval (1998) solar composition. Firstly, we note an average offset of +0.17 dex ($\sigma = 0.07$ dex) in the star-to-star metallicity estimate of Rup106, which can be explained by the difference in the derived effective temperatures. By comparing these two independent results performed on the same dataset, we find agreement with V13 at the 1σ level for Mg, Ti, Sc, Cr, Mn, Zn, Y, La, and Eu, while we note differences up to ~ 0.2 dex for Si, Ca, V, Co, Ni, Cu, and Ba. We attribute these inconsistencies to the different scale adopted for surface gravities and, most importantly, effective temperatures. This comparison proves that diverse assumptions in the procedure to derive chemical abundances make the results of two independent approaches not directly comparable and that the only reliable chemical analysis is within an homogeneous procedure. In general, notwithstanding differences stemming from varied assumptions in the chemical analysis, we reaffirm the distinct chemical characteristics of Rup106 within the MW GC system, alongside the minimal dispersion in chemical abundances among its constituent stars.

Appendix B: Linelist

In Table B.1, we list some useful information about the lines analyzed using the EW method, such as the wavelength, the $\log gf$, the excitation potential (χ) and the EW measured with the code DAOSPEC.

Table B.1. Lines analyzed in this work for each star. The entire table is available in electronic form.

Cluster	Star ID	Element	Wavelength (Å)	log gf	χ (eV)	EW (mÅ)	σ (EW) (mÅ)
NGC 362	1037	Fe I	4804.517	-2.590	3.570	22.20	1.44
NGC 362	1037	Fe I	4807.708	-2.150	3.370	58.80	2.68
NGC 362	1037	Fe I	4808.148	-2.740	3.250	33.90	0.95
NGC 362	1037	Fe I	4813.113	-2.840	3.270	23.40	0.97
NGC 362	1037	Fe I	4867.529	-4.752	1.610	39.80	1.36
NGC 362	1037	Fe I	4869.463	-2.480	3.550	24.70	1.05
NGC 362	1037	Fe I	4882.143	-1.480	3.420	85.60	1.49
NGC 362	1037	Fe I	4918.012	-1.340	4.230	41.60	1.24
NGC 362	1037	Fe I	4927.863	-0.960	4.220	57.20	0.92
NGC 362	1037	Fe I	4950.105	-1.500	3.420	83.20	1.20
...